nature

https://doi.org/10.1038/s41586-024-08493-8

Accelerated Article Preview

Structure and mechanism of the Zorya anti-phage defense system

Received: 17 December 2023

Accepted: 4 December 2024

Accelerated Article Preview

Cite this article as: Hu, H. et al. Structure and mechanism of the Zorya anti-phage defense system. *Nature* https://doi.org/10.1038/s41586-024-08493-8 (2024)

Haidai Hu, Philipp F. Popp, Thomas C. D. Hughes, Aritz Roa-Eguiara, Nicole R. Rutbeek, Freddie J. O. Martin, Ivo Alexander Hendriks, Leighton J. Payne, Yumeng Yan, Dorentina Humolli, Victor Klein-Sousa, Inga Songailiene, Yong Wang, Michael Lund Nielsen, Richard M. Berry, Alexander Harms, Marc Erhardt, Simon A. Jackson & Nicholas M. I. Taylor

Structure and mechanism of the Zorya anti-phage defense system

Haidai Hu[1,10#], Philipp F. Popp[2,10], Thomas C.D. Hughes[3], Aritz Roa-Eguiara[1], Nicole R. Rutbeek[1], Freddie J.O. Martin[1], Ivo Alexander Hendriks[4], Leighton J. Payne[3], Yumeng Yan[1], Dorentina Humolli[5], Victor Klein-Sousa[1], Inga Songailiene[1,6], Yong Wang[7], Michael Lund Nielsen[4], Richard M. Berry[8], Alexander Harms[5], Marc Erhardt[2,9#], Simon A. Jackson[3#], Nicholas M.I. Taylor[1#]

[1]Structural Biology of Molecular Machines Group, Protein Structure & Function Program, Novo Nordisk Foundation Center for Protein Research, Faculty of Health and Medical Sciences, University of Copenhagen, Copenhagen, Denmark.

[2]Institute of Biology/Molecular Microbiology, Humboldt-Universität zu Berlin, Berlin, Germany.

[3]Department of Microbiology and Immunology, University of Otago, Dunedin, New Zealand.

[4]Proteomics program, Novo Nordisk Foundation Center for Protein Research, Faculty of Health and Medical Sciences, University of Copenhagen, Copenhagen, Denmark.

[5]Institute of Food, Nutrition and Health, ETH Zurich, Zurich, Switzerland.

[6]Institute of Biotechnology, Life Sciences Center, Vilnius University, Saulėtekio av. 7, 10257 Vilnius, Lithuania.

[7]College of Life Sciences, Zhejiang University, Hangzhou, China.

[8]Department of Physics and Kavli Institute for Nanoscience Discovery, University of Oxford, Oxford, United Kingdom.

[9]Max Planck Unit for the Science of Pathogens, Berlin, Germany.

[10]These authors contributed equally: Haidai Hu, Philipp F. Popp

#Correspondence: Haidai Hu, haidai.hu@cpr.ku.dk
Marc Erhardt, marc.erhardt@hu-berlin.de
Simon Jackson, simon.jackson@otago.ac.nz
Nicholas Taylor, nicholas.taylor@cpr.ku.dk

Summary

Zorya is a recently identified and widely distributed bacterial immune system that protects bacteria from viral (phage) infections. Three Zorya subtypes have been discovered, each containing predicted membrane-embedded ZorAB complexes paired with soluble subunits that differ among Zorya subtypes, notably ZorC and ZorD in type I Zorya systems[1,2]. Here, we investigate the molecular basis of Zorya defense using cryo-electron microscopy, mutagenesis, fluorescence microscopy, proteomics, and functional studies. We present cryo-EM structures of ZorAB and show that it shares stoichiometry and features of other 5:2 inner membrane ion-driven rotary motors. The $ZorA_5B_2$ complex contains a dimeric ZorB peptidoglycan binding domain and a pentameric α-helical coiled-coil tail made of ZorA that projects approximately 70 nm into the cytoplasm. We also characterize the structure and function of the soluble Zorya components, ZorC and ZorD, finding that they harbour DNA binding and nuclease activity, respectively. Comprehensive functional and mutational analyses demonstrate that all Zorya components work in concert to protect bacterial cells against invading phages. We provide evidence that ZorAB operates as a proton-driven motor that becomes activated upon sensing of phage invasion. Subsequently, ZorAB transfers the phage invasion signal through the ZorA cytoplasmic tail to recruit and activate the soluble ZorC and ZorD effectors, which facilitate degradation of the phage DNA. In summary, our study elucidates the foundational mechanisms of Zorya function as an anti-phage defense system.

Main text

Bacteria face frequent bacteriophage (phage) attacks and have evolved diverse defense strategies, including restriction-modification and CRISPR-Cas systems[3–5]. Anti-phage defense systems play key roles in modulating phage-bacteria population dynamics and have biotechnological potential[6]. Recent studies have identified many new anti-phage defense systems, with further work revealing how some systems are activated by directly sensing phage-encoded proteins, or via indirect mechanisms[1,2,7–10]. Since phage invasion initiates with cell envelope interactions, some defense systems might detect changes in the envelope as early infection signals. However, such defense mechanisms have not yet been discovered.

Among newly discovered anti-phage defense systems, Zorya systems are widespread[1,2]. There are three known Zorya types, each encoding ZorA and ZorB, which are thought to form membrane-embedded complexes related to the proton-driven flagellar stator unit MotAB[11–13]. Additionally, each type encodes one or more cytosolic proteins of unknown function, namely ZorC and ZorD for type I Zorya systems. Most anti-phage defense systems encoding membrane-associated proteins are thought to function by disrupting or depolarizing the host membrane, leading to cell death or dormancy before phage replication completes, a mechanism called abortive infection[14]. A similar membrane-depolarization mechanism for ZorAB has been proposed[1], but it has not been ruled out that ZorAB could instead act as the sensor of infection.

Using single-particle cryo-electron microscopy (cryo-EM), mutagenesis, functional assays, proteomics, and total internal reflection fluorescence (TIRF) microscopy, we decipher several key aspects of the Zorya defense mechanism. We discovered that ZorA and ZorB form a unique 5:2 proton motive force (PMF)-driven motor complex with a long intracellular tail and propose it acts as a phage infection sensor and signal transduction complex. Upon phage perturbation of the cell envelope, the peptidoglycan-binding domain of ZorB anchors the complex to the cell wall, and proton flow drives ZorA and its tail to rotate around ZorB. This rotation induces recruitment of the soluble effectors ZorC and ZorD, which have DNA-binding and nuclease activities, leading to the local degradation of invading phage DNA to facilitate direct (non-abortive) defense.

Zorya protects via a direct mechanism.

Type I Zorya systems are widely distributed across Gram-negative phyla (**Extended Data Fig. 1a-c**). Therefore, we cloned the complete *E. coli* NCTC 9026 type I Zorya system (*Ec*ZorI), including its native promoter, into a low copy plasmid and used a heterologous *E. coli* strain[15] to examine anti-phage defense. The *Ec*ZorI system provided anti-phage activity against a diverse range of phages but some phage families tested were unaffected (**Fig. 1a, b**). *Ec*ZorI did not impair the adsorption of phages to host cells (**Fig. 1c**) but acted subsequently to prevent phage replication and burst (**Fig. 1d**). However, *Ec*ZorI did not defend against plasmids introduced by conjugation or transformation (**Extended Data Fig. 1d, e**), suggesting that some aspect of phage infection, other than the mere introduction of foreign DNA into the cell, triggers Zorya activity.

For population-level defense by *Ec*ZorI in liquid cultures infected at different multiplicities of infection (MOI), each phage tested affected the control populations to differing extents, however population growth in the *Ec*ZorI samples was generally unaffected at low (<0.1) MOI and in some cases also high (>1) MOI (**Fig. 1e** and **Extended Data Fig. 1f, g**). Importantly, the growth kinetics at early timepoints did not reveal any premature host population collapse or delayed growth for cells expressing *Ec*ZorI compared to the negative controls (**Extended Data Fig. 1f**). *Ec*ZorI also reduced the levels of phages detectable at the end timepoints in most infected cultures (**Fig. 1f** and **Extended Data Fig. 1h**). For a single synchronized round of Bas24 infection (at MOI 5), *Ec*ZorI increased the survival rate of infected cells compared to control populations (**Fig. 1g**). Together, these results indicate that *Ec*ZorI acts via a direct rather than abortive infection mechanism. This finding was confirmed using single-cell time-lapse microscopy, where cells expressing *Ec*ZorI continued to replicate after exposure to Bas24, whereas cells lacking *Ec*ZorI lysed within 60 min (**Fig. 1h, i** and **Supplementary Video 1, 2**).

Zorya contains a $ZorA_5B_2$ complex.

To investigate how ZorA and ZorB support direct defense by Zorya, we purified recombinantly expressed *Ec*ZorAB complex from cell membranes using lauryl maltose neopentyl glycol (LMNG) detergent (**Fig. 2a** and **Extended Data Fig. 2a**). Visualized by negative stain EM, *Ec*ZorAB contains a 'head' domain attached to a long 'tail' measuring approximately 700 Å (**Fig. 2b**). We then resolved the *Ec*ZorAB cryo-EM structure to an overall resolution of 2.7 Å, revealing an oligomeric assembly of five ZorA and two ZorB subunits (**Fig. 2c-f**, **Extended Data Fig. 2b-f** and **Extended Data Table 1**). The 5:2 stoichiometry is supported by quantitative mass spectrometry analyses of *Ec*ZorI-expressing cells and conserved with the flagellar stator unit MotAB complex ($MotA_5B_2$) and similar rotary motors[16,17] (**Extended Data Fig. 2g, h** and **Supplementary Table 1**). Overall, *Ec*ZorAB comprises four structural layers: a predicted peptidoglycan binding domain (PGBD, ZorB T47–L246), transmembrane domain (TMD), membrane-proximal cytoplasmic domain (MPCD; spanning ZorA residues G48–L127 and K207–S222), and a tail-like structure formed by the ZorA C-terminal region (ZorA G223–T729) extending into the cytoplasm (**Fig. 2a, c, e**).

The periplasmic domain exhibited flexibility relative to the TMD, accordingly local refinement was used to improve the resolution to 3.5 Å, resolving a dimerized ZorB PGBD (**Extended Data Fig. 2i-k**). Flexibility of the ZorA tail prevented its complete 3D reconstruction, with our cryo-EM map providing density for only the first 56 tail residues, despite the negative stain EM and mass spectrometry analyses confirming the purified complex contained intact full-length ZorA (**Fig. 2b-f**). Secondary structure prediction revealed a preference for the tail to adopt α-helical structures (**Extended Data Fig. 3a**), suggesting that the remaining ZorA tail likely continues the experimentally observed coiled coil with a right-handed super-helical twist. Based on these observations, we constructed an idealized full-length ZorAB model where the ZorA tail forms a helical bundle projecting 70 nm into the cytoplasm, having a helical pitch of 328 Å and a radius of 9.0 Å (**Fig. 2g** and **Extended Data Fig. 3c-e**).

$ZorA_5B_2$ is a PG-binding H^+-driven motor

On the periplasmic side, the C-terminal PGBDs of the ZorB subunits form a homodimer, with the dimerization interface composed of α3 and β5 from each monomer, driven mainly by van der Waals forces and electrostatic interactions. Additionally, a C-terminal loop of ZorB caps the side of the dimerization interface (**Fig. 3a, b** and **Extended Data Fig. 4a, b**). Each monomer contains two disulfide bridges, potentially contributing to the stability and rigidity of this domain: bridges connect α1 to the β1-β2 loop and α3 to the C-terminal loop (**Extended Data Fig. 4b, c**). The overall ZorB dimer structure resembles that of the periplasmic domain of MotB of the flagellar stator unit and of other peptidoglycan (PG)-binding proteins[18–20] (**Extended Data Fig. 4b, d**). MotAB is kept in an inactive state by the MotB 'plug' regions, which are connected via a long linker to the PGBD and inhibit ion flux and rotation of MotA around MotB (**Extended Data Fig. 4e, i-m**). Only upon incorporation of MotAB into the flagellar motor the MotB plug is released and the PGBDs dimerize to enable PG binding[13]. By contrast, the ZorB PGBDs are already dimerized, and the PGBDs are fused without a linker to the ZorB transmembrane helices (TM) through α1 (**Fig. 3a**). Mutations of key residues predicted to be involved in the ZorB PGBD dimer interface, PG binding (Y151, N152, L155 and R159), and the disulfide bridges abolished Zorya-mediated phage defense, as did truncations of the C-terminal loop region (**Fig. 3h** and **Extended Data Fig. 2k, 6a**). *In vitro* pull-down assays demonstrated that purified ZorAB and purified ZorB PGBD bind PG, whereas corresponding PG-binding site mutants displayed reduced binding (**Extended Data Fig. 4f-h, q**). The ZorB TMs are asymmetrically surrounded by five ZorA subunits, each containing three TMs (TM1–TM3). ZorA TM2 and TM3 are lined directly against ZorB TM, while TM1 is peripheral and faces the lipid bilayer. Lipid densities are observed around ZorAB TMD which likely stabilize the TMD (**Fig. 2d**, **Extended Data Fig. 2l**). The ZorAB TMD is structurally related to that of 5:2 ion-driven prokaryotic rotary motors, including possessing the universally conserved and mechanistically essential aspartate residue, D26 in ZorB. One ZorB D26 is engaged with ZorA(3) (ZorA chain 3) via contact with TM2 T147 and TM3 S184 and the other D26 is unengaged and points toward a lumen enclosed by the ZorA MPCD (**Fig. 3a, c**). The interaction modes of these two D26 are the same as those in the inactive state of MotAB[11],

suggesting a similar conformational state and rotary mechanism (**Extended Data Fig. 4i-m**). Despite the lack of a MotB-like 'plug' in ZorB, there are several features potentially blocking the rotation of ZorA around ZorB in this state: ZorA(2) P163 induces a kink in ZorB(1) α1 near residue V46, and two salt bridges, ZorA(2) E164-ZorB(1) R49 and ZorA(5) E164-ZorB(2) R52, and several polar interactions are located at the ZorAB periplasmic assembly interface (**Fig. 3a, d**). Replacing ZorB residues 46–52 with a GGGSGGS linker (to abolish the predicted rotational blockages), then generating a cryo-EM reconstruction revealed that for this mutant, the densities for the ZorB TMs could not be resolved and the ZorB PGBD density is poor, suggesting that ZorA is free to rotate around ZorB (through Brownian motion) in the mutant (**Extended Data Fig. 4n-p, r, s**).

On the cytoplasmic side, the ZorA TMD and MPCD are connected by TM1 and TM3, the intracellular segments of which are joined by three vertical helices (H1-H3) and a β-hairpin motif. H3 is less ordered due to the presence of two proline residues, P126 and P136 (**Extended Data Fig. 5a, b**). We found five strong, spherical densities in the ZorA MPCD, each coordinated by the mainchain carboxylate groups of D217 and Y220 from the end of TM3, and the side chains of E86 and E89 from the adjacent subunit, as well as two well-resolved water molecules. Based on the strongly negative electrostatic environment and the surrounding coordinating residues, we assigned these densities to Ca^{2+}, which bridge the MPCD of two adjacent ZorA subunits and link ZorA TM3 to its intracellular helix (**Fig. 3a, e** and **Extended Data Fig. 5c**). We also observed a water-filled ion permeation pathway connecting the periplasmic space, via the unengaged ZorB D26, to the cytosol (**Fig. 3g**). On the periplasmic side, a cavity lined by several negatively charged residues likely attracts incoming ions. Moving towards the cytoplasmic side, ZorA residues T147 and S184 resemble an ion selectivity filter[21] that controls ion access from the periplasm to ZorB D26 (**Fig. 3c, g**). The absence of the additional polar residues in the ion selectivity filter strictly required for sodium coordination[21] indicates that ZorAB is likely a proton-driven motor (**Extended Data Fig. 4i, k, m**). The pathway extends from ZorB D26 in the direction of the cytoplasm to the inner lumen encircled by the ZorA MPCD, where we found a highly hydrated lateral portal that could facilitate ion exit (**Fig. 3g**).

We next mutated residues along the ion-permeation pathway to probe their role in Zorya defense. ZorB D26 is essential for all models of ion translocation and motor rotation and its mutation to asparagine abolishes Zorya defense. In the ion-selectivity filter, mutation of ZorA T147 or S184 to alanine did not impair Zorya activity against Bas24 but did against other phages, whereas the double mutant ZorA T147/S184 is non-functional against all phages tested. Alanine substitution of ZorA P136, which creates a kink in the ZorA MPCD H3 helix, resulted in increased defense activity against some phages. Furthermore, increasing the side chain size and rigidity of I144, near ZorB D26, which would sterically hinder ZorA from rotating around ZorB, leads to non-functional Zorya (**Fig. g, h** and **Extended Data Fig. 6a, c-e**). We further confirmed the necessity of the PMF-driven ZorAB motor function for Zorya-mediated phage protection by performing single-cell time-

lapse microscopy in the presence or absence of the PMF-dissipating protonophore carbonyl cyanide m-chlorophenyl hydrazone (CCCP). The addition of CCCP did not prevent the growth of cells expressing either *Ec*ZorI or the empty vector control in the absence of phage but did impair *Ec*ZorI-mediated protection against Bas24 (**Fig. 3i, j** and **Supplementary Video 3-6**). These observations support the idea that PMF-driven rotation of ZorA around ZorB is essential for Zorya anti-phage defense.

ZorAB tail controls anti-phage defense

One of the most striking features of the ZorAB complex is its long tail-like structure (**Fig. 2b**, **g**). Within the ZorA MPCD, ZorB N-terminal residues M1 and F2 intertwine and hydrophobically block the entrance of the tail (**Fig. 3a, f**). On the outside of the tail, residue R108 from the β-hairpin motif forms a salt bridge with E227, and H92 makes electrostatic contact with the hydroxyl group of Y228 (**Extended Data Fig. 5c**). Disrupting these interactions leads to loss of defense against Bas24 (**Fig. 3h**). Inside the tail, L250, L254, L258 and L261 from each ZorA subunit make up continuous hydrophobic pentameric rings. Additionally, we observed an extra density along the tail central axis in this region, which is best modeled as a fatty acid, consistent with a predicted lipid binding site[22] (**Extended Data Fig. 5d, f**). Mutants targeting this hydrophobic motif abolished Zorya defense (**Fig. 3h**) and we observed that although the tail bundle appeared assembled in purified ZorA$^{L250G/L254G/L258G/L261G}$ZorB and ZorA$^{L250N/L254N/L258N/L261N}$ZorB mutants, the TMD domain was perturbed (**Extended Data Fig. 5g, h**), suggesting that the ZorA tail influences correct ZorAB TMD assembly. To further test this, we deleted the entire tail (ZorA$^{\Delta 223-729}$) and this mutant also abolished ZorAB TMD motor formation (**Extended Data Fig. 5i**). Given that the tail structure protrudes into the cytoplasm and is surrounded by aqueous solution, hydrophobic interactions inside the tail seem to be the primary driving force for tail assembly, and it is unlikely that the tail conducts ions or other small soluble molecules (**Extended Data Fig. 3d, e**). Intriguingly, part of the ZorA tail (residues 540-729) shows homology with the core signaling unit of the bacterial chemosensory array (**Extended Data Fig. 3b**), which contains a long intracellular helical bundle responsible for transferring signal from the extracellular environment into the cell and regulates the activities of the subsequent effectors[23]. Sequence analyses further reveal that long ZorA tails are present in all Zorya subtypes, suggesting that tail length is functionally important (**Extended Data Fig. 6b**).

Deletion of any of the Zorya genes results in loss of anti-phage defense, emphasizing that the complete function of the Zorya system requires communication between the membrane-anchored ZorAB complex and cytosolic soluble proteins (**Fig. 3h** and **Fig. 4c, i**). Considering the motor-like structural features of ZorAB TMD and its long cytoplasmic tail, we speculated that the ZorA tail is responsible for transmitting a signal derived from the activated ZorAB motor to the cytosolic proteins ZorC and ZorD. To test whether the length of the ZorA tail is important for Zorya function, we made four ZorA tail truncations: deleting the beginning (ZorA$^{\Delta 223-482}$), middle (ZorA$^{\Delta 359-592}$) and tip (ZorA$^{\Delta 483-729}$) of the tail as well as a combination of deleting the beginning

and tip (ZorA$^{\Delta 223\text{-}343/\Delta 449\text{-}729}$) (**Extended Data Fig. 5a**). Purification and cryo-EM analyses of ZorA$^{\Delta 359\text{-}592}$ ZorB and ZorA$^{\Delta 435\text{-}729}$ ZorB confirmed that the deletions resulted in shorter tails but did not impair ZorAB TMD motor assembly (**Extended Data Fig. 5j-m** and **Extended Data Table 1**). However, all tail truncations abolished Zorya defense (**Fig 3h** and **Extended Data Fig. 6a, c, d**). Mutating the Ca^{2+} binding site (E86A and E89A) also resulted in loss of Zorya function (**Fig. 3h** and **Extended Data Fig. 6a**) and caused conformational changes in the ZorA MPCD, including to the linker between TM3 and ZorA tail helix (**Extended Data Fig. 5e, n**). Therefore, inactivation of the Ca^{2+} binding sites likely disrupts the connection between the ZorAB TMD motor and the tail. These data indicate that ZorAB tail integrity and its motor connection are essential for Zorya anti-phage activity, supporting the role of the ZorA tail in communicating with the cytosolic effector proteins.

ZorC/D DNA interactions enable defense

To better understand the roles of ZorC and ZorD in anti-phage defense, we next obtained their structures and investigated their biological roles. ZorC possesses a domain containing an EH signature motif (E400, H443) with unknown function. We determined the cryo-EM structure of *Ec*ZorC to an anisotropic resolution of 3.7 Å, with sufficient density to model residues R58–P478 (**Fig. 4a, Extended Data Fig. 7a-e** and **Extended Data Table 1**). *Ec*ZorC consists of a 'core' domain that connects through a long linker to a C-terminal globular domain, the density of which is blurred, and *de novo* model building was not possible (**Extended Data Fig. 7b**). In the core domain, the EH signature motif E400 and H443, together with D332, R335, W339, and W458, form an electrostatic network (**Fig. 4b**). Additionally, in an AlphaFold3[24]-predicted full-length ZorC model, the N-terminal region (residues M1–E48) was modeled with low confidence as two hydrophilic helices that extend from the core domain beyond the density observed in the cryo-EM map (**Extended Data Fig. 7b, f**). Deletion of the N-terminal helices or the C-terminal globular domain results in loss of Zorya function (**Fig. 4c**). The ZorC surface contains several patches of net positive charge, including the region containing the EH signature motif (**Extended Data Fig. 7g**), suggesting that ZorC might interact with nucleic acids. Using electrophoretic mobility shift assays (EMSAs), we observed that ZorC can bind dsDNA in a sequence-independent manner (**Fig. 4d** and **Extended Data Fig. 7h**). Both the EH signature motif and C-terminal globular domain are required for ZorC DNA binding activity (**Fig. 4e**). We further confirmed the ZorC-DNA binding by obtaining a cryo-EM dataset of ZorC in complex with dsDNA. Although we did not obtain a high-resolution reconstruction, the 2D classes clearly indicate that the EH motif containing domain interacts with DNA (**Fig. 4f** and **Extended Data Fig. 7i**). Further, ZorC E400A or H443A mutations abolished Zorya function, indicating that ZorC DNA binding is indispensable for Zorya defense (**Fig. 4c** and **Extended Data Fig. 6a**).

*Ec*ZorD contains a predicted Snf2-related domain at its C-terminus and such domains are known to use ATP hydrolysis to bind or remodel DNA[25]. Therefore, we determined the structure of *Ec*ZorD in the absence and presence of a slowly hydrolysable ATP analog, ATP-γ-S (**Fig. 4g**,

Extended Data Fig. 8a-d and **Extended Data Table 1**). The *Ec*ZorD N-terminal domain (residues M1–N502) interacts directly with its C-terminal domain (residues D503–A1080), forming a toroid-shaped molecule. ATP-γ-S is bound within a cleft near the hallmark DEAQ box motif (ZorD residues D730-Q733), surrounded by many conserved negatively charged residues (**Fig. 4h**). Mutations in both the ATP binding site (D730A/E731A) and those conserved negatively charged residues resulted in loss of Zorya function (**Fig. 4i**). We next assessed ZorD DNA targeting activity by incubating purified ZorD with plasmid DNA *in vitro*. Full-length ZorD was unable to degrade DNA, however, the ZorD C-terminal domain exhibited nuclease activity and rapidly degraded both plasmid DNA and phage genomic DNA (**Fig. 4j, k** and **Extended Data Fig. 8e)**. Mutating the DEAQ box motif (D730A, E731A) or a glutamate (E651) recognizing the ATP ribose group completely abolished the nuclease activity of the ZorD C-terminal domain (**Fig. 4j**). In addition, the presence of ZorC did not activate the autoinhibited ZorD nuclease activity, nor inhibited the activity of the ZorD C-terminal nuclease domain (**Extended Data Fig. 8f, g**). This aligns with the finding that ZorC and/or ZorD alone cannot protect against phage infection without ZorAB. Our results suggest that ZorD has nuclease activity and that its full-length form is autoinhibited, likely becoming active once defense is triggered, presumably through a conformational change consistent with AlphaFold3 predictions. (**Extended Data Fig. 8h-m**).

To directly measure ZorD nuclease activity *in vivo*, we attempted to use the *parS*-ParB system to track phage DNA within infected cells[26]. While the system was not functional with Bas24, we were able to establish activity with Bas54, against which Zorya also confers protection (**Fig. 1b**). Using time-lapse microscopy to track the presence of phage DNA during Bas54::*parS* infection, we observed Bas54::*parS* DNA within infected cells (detected as fluorescent spots of ParB-mScarlet bound to *parS* loci) in the absence but not presence of Zorya (**Extended Data Fig. 7j** and **Supplementary Video 7**). This supports our model for Zorya-mediated phage DNA degradation, but could also be explained if Zorya blocked injection of phage DNA. To exclude this possibility, we labelled Bas24 phage DNA with a fluorescent dye (SYTOX Orange) and used time-lapse imaging to track phage adsorption, DNA injection, and subsequent fate of the injected DNA and infected cells. In the absence of Zorya, we observed individual phage particles adsorbing and injecting their DNA, apparent as transfer of fluorescence from the phage capsid to an accumulation of intracellular fluorescence. In the presence of Zorya, DNA injection still occurred (the fluorescence from the adsorbed phage particles decreased over time, consistent with the rate of DNA injection in the absence of Zorya), but we detected no intracellular fluorescence accumulation, suggesting the injected phage DNA was rapidly degraded, and the cells were protected from lysis (**Fig. 4l-n** and **Supplementary Video 8**). These experiments provide further evidence supporting phage DNA degradation by the *Ec*ZorI system.

ZorAB recruits ZorC/D during phage invasion

We next examined how ZorAB, ZorC, and ZorD coordinate during phage infection. We explored whether *zorC* and *zorD* from a *Pseudomonas aeruginosa* type I Zorya system could complement

corresponding deletions of *Ec*ZorI genes, but this was not the case, suggesting that direct interactions occur between ZorAB and either or both ZorC or ZorD (**Extended Data Fig. 9a, b**). Additionally, quantitative mass spectrometry of *Ec*ZorI-expressing cells implied an approximate 1:1:1 $ZorA_5B_2$:ZorC:ZorD stoichiometry (**Extended Data Fig. 2g, h**). We then used TIRF microscopy to examine the sub-cellular distributions of functional mNeonGreen (mNG) or HaloTag (HT) fusions to ZorB, ZorC and ZorD (**Extended Data Fig. 9c, d**). In the presence and absence of phage, ZorB-mNG and ZorB-HT formed distinct membrane-associated foci, while expression of mNG alone from the *Ec*ZorI promoter resulted in uniform, cytoplasmic fluorescence independent of phage (**Fig. 5a, c** and **Extended Data Fig. 9e, f**). We observed a slight but significant increase in ZorB-mNG foci in phage-infected bacteria, which was independent of ZorAB motor function, as the non-rotating $ZorB^{D26N}$ mutant showed a similar increase (**Fig. 5a, b**). For both mNG-ZorC and ZorD-mNG, we observed a significant increase in membrane-associated foci formation upon phage infection compared to the non-phage control, suggesting that the cytosolic effector proteins ZorC and ZorD are recruited to an activated *Ec*ZorI system (**Fig. 5c, d**). This result is reinforced by a positive correlation between the number of ZorD foci and the phage MOI (**Extended Data Fig. 9h, i**). We then used dual-tagged constructs to investigate co-localization of ZorB-HT with either mNG-tagged ZorC or ZorD (**Extended Data Fig. 9c**). In the absence of phage, ZorB and ZorC or ZorD foci rarely co-localized. However, upon Bas24 infection, co-localization of ZorC-mNG or ZorD-mNG with ZorB-HT occurred in approximately 20% or 30% of cells, respectively (**Fig. 5e-h**). Since TIRF microscopy visualizes only about a quarter of the cell depth[27], the observed co-localization is likely an under-representation of the ZorC/D recruitment frequency. No ZorD co-localization was detected in the non-functional motor $ZorB^{D26N}$ mutant or in a ZorA tail tip deletion mutant (**Fig. 5h**). Overall, these data suggest that the cytosolic effector proteins ZorC and ZorD are recruited to phage-activated ZorAB complexes, and that both the rotary function of ZorAB and the cytoplasmic tail of ZorA are required to transmit the phage infection signal and recruit the cytosolic nuclease to activated ZorAB.

Discussion

We show that an *E. coli* type I Zorya system exhibits defense activity against phylogenetically diverse phages through a direct immunity mechanism but not against bacterial conjugation or plasmid transformation. ZorA and ZorB form an inner membrane-integrated $ZorA_5B_2$ proton-driven rotary motor complex with a long, intracellular tail structure. We propose that the ZorAB complex acts as a sensor to detect phage infection and transmits the invasion signal, via rotation of the ZorA tail, to recruit and activate the effectors ZorC and ZorD, which bind and degrade invading phage DNA (**Fig. 5i-k**). Our model and data refute a previous hypothesis that ZorC and ZorD are involved in sensing and inactivation of phage DNA, with ZorAB acting as a proton channel to depolarize the membrane potential and induce cell death if the initial ZorC/D protection failed[1]. Instead, we found that the defense is direct, does not induce cell dormancy or death, and that ZorC and ZorD alone (without ZorAB) do not provide protection from phage infection.

We propose that ZorAB senses phage-induced perturbations that reduce the distance between the inner membrane (IM) and the PG layer, allowing ZorB to anchor to PG. PG binding and ion flow through the transmembrane domain are essential for ZorAB and the flagellar stator unit MotAB to function as rotary motors. However, the short distance of the ZorB PGBD to the membrane motor unit (due to the absence of a flexible linker typical for MotB) means that normally, the PG layer is too distant for ZorB to reach (**Fig. 3a** and **Extended Data Fig. 4e**). Therefore, we propose that ZorAB complexes are usually inactive and free to diffuse laterally, as observed for MotAB complexes before flagellar incorporation[13,28]. Perturbation of the PG layer or an increase in local curvature of the IM (known to occur during breaching of the cell envelope by some phages)[29], or other phage-induced cell envelope changes that reduce the IM-PG layer distance (such as localized PG degradation generating 'frayed' edges)[30], would enable the ZorB PGBD to contact the PG layer, allowing binding and subsequent activation of ZorAB and recruitment and/or activation of effectors (ZorC and ZorD) to clear the phage infection (**Fig. 5i-k**). Interestingly, although flagellar stator units are widely distributed among both Gram-positive and Gram-negative bacteria[13], Zorya is underrepresented in bacteria with single-membrane cell envelopes, which suggests that differences in cell wall architecture or phage infection mechanisms might prevent effective phage-induced activation of Zorya (**Extended Data Fig. 1a-c**).

Sensing perturbation of the cell envelope provides an elegant mechanism that exploits the critical early stages of infection to trigger a direct anti-viral defense. While the exact mechanism of phage-induced ZorAB anchoring and activation remains to be uncovered, the need of a rotary motor and the long ZorA tail to recruit and activate effectors suggests an intriguing hypothesis in which the effectors (ZorC/ZorD) are specifically activated in close proximity to the cell membrane. This localized effector function would protect host DNA from effector activity without relying on epigenetic-based self vs. non-self discrimination mechanisms[31] (**Supplementary Discussion**).

Overall, we provide structural and functional insight into the Zorya defense system and propose that Zorya acts early in infection by sensing perturbation of the cell envelope to initiate a localized

anti-phage response near the cell membrane. Our work paves the way for further research to understand the detailed mechanisms of this unique activation signal for anti-phage defense.

Main text references:

1. Doron, S. *et al.* Systematic discovery of antiphage defense systems in the microbial pangenome. *Science* **359**, (2018).

2. Payne, L. J. *et al.* Identification and classification of antiviral defence systems in bacteria and archaea with PADLOC reveals new system types. *Nucleic Acids Res.* **49**, 10868–10878 (2021).

3. Smith, W. P. J., Wucher, B. R., Nadell, C. D. & Foster, K. R. Bacterial defences: mechanisms, evolution and antimicrobial resistance. *Nat. Rev. Microbiol.* **21**, 519–534 (2023).

4. Bernheim, A. & Sorek, R. The pan-immune system of bacteria: antiviral defence as a community resource. *Nat. Rev. Microbiol.* **18**, 113–119 (2020).

5. Hampton, H. G., Watson, B. N. J. & Fineran, P. C. The arms race between bacteria and their phage foes. *Nature* **577**, 327–336 (2020).

6. Wang, J. Y. & Doudna, J. A. CRISPR technology: A decade of genome editing is only the beginning. *Science* **379**, eadd8643 (2023).

7. Gao, L. *et al.* Diverse enzymatic activities mediate antiviral immunity in prokaryotes. *Science* **369**, 1077–1084 (2020).

8. Millman, A. *et al.* An expanded arsenal of immune systems that protect bacteria from phages. *Cell Host Microbe* (2022) doi:10.1016/j.chom.2022.09.017.

9. Stokar-Avihail, A. *et al.* Discovery of phage determinants that confer sensitivity to bacterial immune systems. *Cell* **186**, 1863-1876.e16 (2023).

10. Vassallo, C. N., Doering, C. R., Littlehale, M. L., Teodoro, G. I. C. & Laub, M. T. A functional selection reveals previously undetected anti-phage defence systems in the E. coli pangenome. *Nat. Microbiol.* **7**, 1568–1579 (2022).

11. Santiveri, M. *et al.* Structure and Function of Stator Units of the Bacterial Flagellar Motor. *Cell* (2020) doi:10.1016/j.cell.2020.08.016.

12. Deme, J. C. *et al.* Structures of the stator complex that drives rotation of the bacterial flagellum. *Nat. Microbiol.* **5**, 1553–1564 (2020).

13. Hu, H. *et al.* Structural basis of torque generation in the bi-directional bacterial flagellar motor. *Trends Biochem. Sci.* **0**, (2021).

14. Rousset, F. & Sorek, R. The evolutionary success of regulated cell death in bacterial immunity. *Curr. Opin. Microbiol.* **74**, 102312 (2023).

15. Maffei, E. *et al.* Systematic exploration of Escherichia coli phage–host interactions with the BASEL phage collection. *PLOS Biol.* **19**, e3001424 (2021).

16. Rieu, M., Krutyholowa, R., Taylor, N. M. I. & Berry, R. M. A new class of biological ion-driven rotary molecular motors with 5:2 symmetry. *Front. Microbiol.* **13**, (2022).

17. Martin, F. J. O., Santiveri, M., Hu, H. & Taylor, N. M. I. Ion-driven rotary membrane motors: From structure to function. *Curr. Opin. Struct. Biol.* **88**, 102884 (2024).

18. Roujeinikova, A. Crystal structure of the cell wall anchor domain of MotB, a stator component of the bacterial flagellar motor: Implications for peptidoglycan recognition. *Proc. Natl. Acad. Sci.* **105**, 10348–10353 (2008).

19. Zhu, S. *et al.* Conformational change in the periplamic region of the flagellar stator coupled with the assembly around the rotor. *Proc. Natl. Acad. Sci.* **111**, 13523–13528 (2014).

20. Trinh, N. T. T. *et al.* Crystal structure of Type IX secretion system PorE C-terminal domain from Porphyromonas gingivalis in complex with a peptidoglycan fragment. *Sci. Rep.* **10**, 7384 (2020).

21. Hu, H. *et al.* Ion selectivity and rotor coupling of the Vibrio flagellar sodium-driven stator unit. *Nat. Commun.* **14**, 4411 (2023).

22. Krapp, L. F., Abriata, L. A., Cortés Rodriguez, F. & Dal Peraro, M. PeSTo: parameter-free geometric deep learning for accurate prediction of protein binding interfaces. *Nat. Commun.* **14**, 2175 (2023).

23. Riechmann, C. & Zhang, P. Recent structural advances in bacterial chemotaxis signalling. *Curr. Opin. Struct. Biol.* **79**, 102565 (2023).

24. Abramson, J. *et al.* Accurate structure prediction of biomolecular interactions with AlphaFold 3. *Nature* **630**, 493–500 (2024).

25. Dürr, H., Flaus, A., Owen-Hughes, T. & Hopfner, K.-P. Snf2 family ATPases and DExx box helicases: differences and unifying concepts from high-resolution crystal structures. *Nucleic Acids Res.* **34**, 4160–4167 (2006).

26. Owen, S. V. *et al.* Prophages encode phage-defense systems with cognate self-immunity. *Cell Host Microbe* **29**, 1620-1633.e8 (2021).

27. Mattheyses, A. L., Simon, S. M. & Rappoport, J. Z. Imaging with total internal reflection fluorescence microscopy for the cell biologist. *J. Cell Sci.* **123**, 3621 (2010).

28. Wadhwa, N. & Berg, H. C. Bacterial motility: machinery and mechanisms. *Nat. Rev. Microbiol.* 1–13 (2021) doi:10.1038/s41579-021-00626-4.

29. Hu, B., Margolin, W., Molineux, I. J. & Liu, J. Structural remodeling of bacteriophage T4 and host membranes during infection initiation. *Proc. Natl. Acad. Sci.* **112**, E4919–E4928 (2015).

30. Latka, A., Maciejewska, B., Majkowska-Skrobek, G., Briers, Y. & Drulis-Kawa, Z. Bacteriophage-encoded virion-associated enzymes to overcome the carbohydrate barriers during the infection process. *Appl. Microbiol. Biotechnol.* **101**, 3103–3119 (2017).

467 31. Samson, J. E., Magadán, A. H., Sabri, M. & Moineau, S. Revenge of the phages: defeating
468 bacterial defences. *Nat. Rev. Microbiol.* **11**, 675–687 (2013).

Figure Legends:

Figure 1. Zorya has broad activity against phages via a direct immunity mechanism.
a, Schematic representation of *Ec*ZorI operon. **b**, *Ec*ZorI defense against diverse *E. coli* phages, determined using efficiency of plaquing (EOP) assays. AAI: Average amino acid identity between proteins encoded by each phage (providing an estimate of the relatedness between phages). **c**, Adsorption of phage Bas24 to *E. coli* cells possessing or lacking *Ec*ZorI. **d**, One-step phage growth curve for phage Bas24 infecting *E.coli*, with or without *Ec*ZorI, normalized to the plaque forming units (PFU) per mL at the initial timepoint. **e**, Infection time courses for liquid cultures of *E. coli*, with and without *Ec*ZorI, infected at different multiplicities of infection (MOI) of phage Bas24. **f**, Phage titers at the end timepoint for each sample from the infection time courses (**e**), measured as PFU/mL on indicator lawns of *E. coli* either without (control) or with *Ec*ZorI. The limit of detection (LOD) is shown with dotted lines. **g**, Survival of *E. coli* cells, lacking or possessing *Ec*ZorI, infected at an MOI of 5 with Bas24. **h**, Time-lapse, phase-contrast microscopy of *E. coli* cells with and without *Ec*ZorI infected with Bas24 at an MOI of 5. **i**, Quantitation of the time-lapse microscopy in (**h**), displaying the measured cell area relative to the initial timepoint. In panels **b-g**, data represent the mean of at least three biological replicates (data points indicate replicates) and error bars (**c, d**) or shaded regions (**e**) represent the standard error of the mean (SEM). Means and standard deviation shown in **i** derives from independent biological triplicates.

Figure 2. Cryo-EM of *Ec*ZorAB and its architecture.
a, Schematic representation of *Ec*ZorA and *Ec*ZorB. **b,** Negative stain EM image of purified *Ec*ZorAB particles. **c**, Representatives of high-resolution 2-dimensional classes of *Ec*ZorAB images from cryo-EM. Domain architectures of the E*c*ZorAB complex are depicted. **d**, Cryo-EM map of *Ec*ZorAB. Five ZorA subunits (purple, salmon, light green, tan, and coral) surround two ZorB subunits (white and dark gray) viewed from the plane of the membrane. Membrane-bound lipids are shown in yellow. The detergent micelle is shown as a translucent surface representation in cyan. Dashed lines depict inner membrane boundaries. Two cross-section views of *Ec*ZorAB TMD and tail are shown. **e**, Cross-section view of the EM density map from the plane of the membrane. **f**, Ribbon model representation of *Ec*ZorAB, with two cross-section views of the model shown. **g**, Composite model of *Ec*ZorAB whole complex, represented as surface. The radius of the ZorA tail is indicated. PP, periplasm; IM, inner membrane; CP, cytoplasm; PGBD, peptidoglycan binding domain; TMD, transmembrane domain; MPCD, membrane-proximal cytoplasmic domain; TM, transmembrane; H, helix. Images in **b** is representative of at least 3 replicates.

Figure 3. ZorAB is a PG-binding, proton-driven motor.
a, *Ec*ZorAB viewed from the plane of the membrane, with ZorB shown as ribbons (black and white) and ZorA shown as a translucent surface. The distance between the inner membrane and PG layer in *E.coli* is approximately 90 Å[76]. The cysteines from the two disulfide bridges in the ZorB PGBD are indicated and shown as spheres. The aspartate residues D26 from both ZorB TM

are indicated and shown. **b**, Top view of the ZorB PGBD. **c,** Cross section view of ZorAB TMD, showing the ZorB D26 and surrounding residues. **d,** Close-up view of the interactions of ZorB with ZorA at the domain assembly interface in the periplasmic space. **e**, Ca^{2+} binding site. EM densities are only overlapped on Ca^{2+} ion, and the two water molecules. **f**, Close-up view of the interactions of the ZorB N-terminus with ZorA tail **g**, Ion translocation pathway (semitransparent surface representation in light blue) in ZorAB. Residues along the ion permeation pathway and from the ion selectivity filter are shown. Each asterisk indicates residues or structural elements from the neighboring ZorA subunit. **h**, The effects of ZorA and ZorB mutations on *Ec*ZorI-mediated anti-phage defense against Bas24, as measured using EOP assays. Data represent the mean of at least 3 replicates (data points indicate replicates) and are normalized to the control samples lacking *Ec*ZorI. $ZorB^{46\text{-}52>GGGSGGS}$ corresponds to the replacement of ZorB residues 46-52 with a GGGSGGS linker. Data for additional phages are provided in **Extended Data Fig. 6a**. **i**, Time-lapse, phase contrast microscopy of *E. coli* cells expressing empty vector control or *Ec*ZorI with or without exposed to Bas24 at an MOI of 5 in the presence or absence of 30 μM CCCP. **j**, Quantitation of the time-lapse microscopy in (i), displaying the measured cell area relative to the initial timepoint images. Means and standard deviation shown in **i** derives from independent biological triplicates.

Figure 4. Structural and functional characterization of ZorC and ZorD.

a, Ribbon model representation of ZorC. Residues from R58 to P478 were modeled based on EM density. **b**, Details of the ZorC EH signature motif. **c**, Effects of ZorC mutations on *Ec*ZorI-mediated anti-phage defense, as measured using EOP assays. **d**, *In vitro* interaction of *Ec*ZorC with 200 nM dsDNA (18bp, 50% GC content, 5' FAM-labeled dsDNA, sequence in **Extended Data Fig. 7h**), ZorC concentrations were from lane 1 and 3 to lane 7: 2500, 100, 250, 500, 1000, and 2500 nM, respectively. **e**, The effects of ZorC mutations on dsDNA binding activity, all reactions were made to a final concentration of 100 nM of dsDNA and 2000 nM of protein. **f**, Representatives of high-resolution 2-dimensional classes of *Ec*ZorC *apo* and *Ec*ZorC-dsDNA complex images from cryo-EM. **g**, Ribbon model representation of *Ec*ZorD in complex with ATP-γ-S, with the bound ATP-γ-S shown in sphere representation. **h**, Details of ATP-γ-S binding sites. The backbone of the DEAQ box motif (ZorD residues 730-733) is colored in magenta. Conserved negatively charged residues surrounding DEAQ box motif is shown. **i**, The effects of ZorD mutations on *Ec*ZorI-mediated anti-phage defense, as measured using EOP assays. ΔNTD represents $ZorD^{\Delta 1\text{-}502}$ and ΔCTD represents $ZorD^{\Delta 503\text{-}1080}$. For **c** and **i**, data represent the mean of at least 3 replicates (data points indicate replicates) and are normalized to the control samples lacking *Ec*ZorI. Data for additional phages are provided in **Extended Data Fig. 6a**. **j**, $ZorD_{CTD}$ degrades linear plasmid DNA. **k**, $ZorD_{CTD}$ degrades phage Bas24 genomic DNA (gDNA). Data for additional phages are provided in **Extended Data Fig. 8e. l**, Time-lapse montage of SYTOX Orange-labeled Bas24 infections. Arrows indicate phage particles that appear to adsorb and inject their DNA. **m**, Schematic showing the apparent transfer of labelled phage DNA from the capsid to inside the cell. **n**, Quantification of intracellular fluorescence levels over time in individual *E.*

coli cells, comparing the infection dynamics in Zorya-deficient cells and *Ec*ZorI-expressing cells (data from panel l, plus four additional replicates). Dotted points indicate cell lysis of *E. coli* cells lacking *Ec*ZorI. Bold lines represent the mean estimated from a linear regression analysis. Images in **d**, **e**, **j**, **k** are representatives of at least 3 replicates.

Figure 5. Sub-cellular distributions and co-localization of Zorya components with a proposed model.

a, Exemplary denoised TIRF images of sub-cellular distributions of $ZorB^{WT}$ and $ZorB^{D26N}$ fused to HaloTag (HT) with and without Bas24 (± Bas24). Scale bar 1 μm. **b**, Comparison of detected maxima of the ZorAB complex foci between untreated or exposed to Bas24 (MOI 5, 30 min; n cells > 250, 3 replicates). P-values: 0.022 and 0.027. **c**, Exemplary denoised TIRF images of sub-cellular distributions of mNG-tagged ZorC and ZorD ±Bas24; mNG was fused to either the ZorC N-terminus (mNG-ZorC) or ZorD C-terminus (ZorD-mNG). Scale bar 1 μm. **d**, Comparison of detected maxima of the ZorC and ZorD foci between untreated or exposed to Bas24 (MOI 5, 30 min; n cells > 250). P-values: 0.004 and 0.04. **e**, Exemplary denoised TIRF images of co-localization of mNG-ZorC with $ZorB^{WT}$-HT ± Bas24. Scale bar 1 μm. White arrows highlight co-localization. **f**, Co-localization analysis of ZorB-HT wildtype or a mutant $ZorB^{D26N}$ with ZorC-mNG ± Bas24 (MOI 5, 30 min). P-values: 0.0002, 0.0042. **g**, Exemplary denoised TIRF images of co-localization of ZorD-mNG with ZorB-HT ± Bas24. Scale bar 1 μm. **h**, Co-localization analysis of ZorB-HT wildtype or mutants ($ZorB^{D26N}$ and ZorA tail tip deletion Δ483-739) with ZorD-mNG ± Bas24 (MOI 5, 30 min). P-values: <0.0001 and <0.0001. **i-k**, Proposed Zorya defense model: **i**, Inactive ZorAB diffuse laterally withing the IM. **j**, Inactive ZorAB detect cell envelop perturbation during phage infectionZorB PGBDs anchor to PG. Ion translocation through ZorAB triggers ZorA and its tail to rotate around ZorB. **k**, ZorAB motor signal is transferred through the ZorA tail, which recruits and/or activates ZorC and ZorD that bind and degrade phage DNA, preventing phage replication. Data points represent the mean foci counts for each of three replicates and the shaded bars represent the mean between replicates. For **b** and **d** data are presented as mean values with min to max whiskers. Statistical tests were performed using unpaired t-tests or two-way ANOVA for **b**, **d** and **f**[59]. P-value: GP Prism style, 0.12 ns, 0.04 (*), 0.009 (**), 0.0009 (***), <0.00009 (****).$ZorB^{WT}$-HT and $ZorB^{D26N}$-HT expression data are provided in **Extended Data Fig. 6e**.

Methods

Phylogenetic analysis of Zorya systems

To create the phylogenetic tree shown in **Extended Data Figure 1b**, Zorya systems were identified by running PADLOC[32] v1.1.0 with PADLOC-DB v1.4.0 across RefSeq v209 bacterial genomes[33]. For a representative sample of high-quality Zorya systems, the results were filtered for systems with canonical gene order (*zorABCD*, *zorABE*, or *zorFABG* for types I, II, and III, respectively), which were not at the edge of a contig, and where the ZorA protein had minimum PADLOC-DB target and hmm alignment coverages of 80%. The respective ZorA sequences were trimmed to 250 amino acids to roughly isolate the 'head' domain (representing the TMD motor unit). The ZorA head sequences were then clustered using MMseqs2[34] v15.6f452 with options: --min-seq-id 0.8 --coverage 0.8, and the representative sequences for each resulting cluster were used for subsequent analyses. For the representative ZorA sequences, a diversified ensemble of 100 replicate alignments was built using the Super5 algorithm of muscle v5.1[35] by perturbing each guide tree with 25 different seeds. *Escherichia coli* MotA (WP_000906340.1) was included in the alignments as an outgroup. The alignment with the greatest column confidence was used to build a phylogenetic tree with FastTree v2.1.11 with options: -lg[36]. Bacteria encoding each protein were assigned taxonomy based on GTDB v214.1[37], grouping phyla with alphabetic suffixes into their base phylum. To create the phylogenetic tree shown in **Extended Data Figure 1c**, the GTDB v214.1 bacterial reference tree was filtered for genomes present in RefSeq v209 and collapsed to the phylum level.

Cloning of Zorya defense system and mutagenesis

The *Ec*ZorI operon with its native promoter region was amplified by PCR from the *E. coli* strain NCTC9026 genome (purchased from the National Collection of Type Cultures, NCTC) and subcloned into a modified pACYC vector using In-Fusion cloning strategy (In-Fusion® Snap Assembly Master Mix; TaKaRa Cat. # 638947). The *Pa*ZorI operon was amplified from the *P. aeruginosa* strain DSM24068 genome (DSMZ-German Collection of Microorganisms and Cell Cultures GmbH; Leibniz Institute) and was subcloned into a modified pACYC vector under the *E. coli* ZorI native promotor using In-Fusion cloning strategy. For generating mutations (point mutations, deletions, mNeonGreen or Halo tag insertions, of where *Ec*ZorI *zorC* or *zorCD* genes were replaced by *Pa*ZorI *zorC* or *zorCD*), plasmids were constructed based on standard cloning techniques (In-fusion snap assembly). All plasmids were verified by either Sanger or nanopore sequencing.

Phage infectivity assays

The host *E. coli* ΔRM (hereafter ΔRM, a derivative of *E. coli* MG1655 engineered to remove multiple restriction modification systems, which was used isolate the BASEL phage collection)[15], possessing either pControl (pACYC) or p*Ec*ZorI (or mutants thereof) were grown overnight in LB + Chloramphenicol (Cm; 25 μg/mL). Efficiency of plaquing (EOP) assays were performed using bacterial lawns of the host strain in 0.35% LB agar + 10 mM $MgSO_4$ + 2 mM $CaCl_2$ overlaid onto 1.5% LB agar + Cm. Ten-fold dilution series of phages were spotted onto the overlays, air-dried, then the plates were incubated overnight at 30°C. Liquid culture infection time courses were performed in 96-well plates in an incubated shaking plate reader at 30°C. The time courses were begun with cells at an OD_{600} of 0.05 and phages were added at the indicated MOI, assuming an OD_{600} to cell ratio of 3×10^8 cells per OD_{600} unit. Average amino acid identity (AAI) between phages (indicative of relatedness) and hierarchical clustering of phage genomes was calculated using EzAAI[38], separating clusters with proteome coverage <40%.

Phage adsorption and one-step growth curves assays

Overnight cultures of ΔRM possessing either pControl or p*Ec*ZorI were used to inoculate fresh LB + Cm cultures at a 1:100 dilution. The inoculated cultures were grown at 30°C with shaking until reaching an OD_{600} of 0.4–0.6, then harvested by centrifugation, washed with LB + Cm, and resuspended at an OD_{600} of 1.0 in LB + 10 mM $MgSO_4$ + 2 mM $CaCl_2$. For phage adsorption assays, 10 mL samples of resuspended cells were infected with phage Bas24 at an MOI of 10^{-4}, then the samples were mixed and incubated at 30°C without shaking. For the 0 min timepoint (total input phages), 100 μL samples were removed and added to 0.35% LB Agar seeded with ΔRM + pControl (as an indicator lawn), then poured on top of 1.5% LB agar + Cm. For each subsequent time point, 1 mL samples were taken, centrifuged to pellet cells, then the supernatant (containing unabsorbed phages) was filtered through a 0.2 μm PES syringe filter. Samples (100 μL) of the filtered supernatant were added to indicator overlays (as above) poured onto 1.5% LB agar + Cm. All overlay plates were incubated overnight at 30°C before counting plaques. For each timepoint, the percentage of unabsorbed phages was calculated as the timepoint plaque count / plaque count for the time 0 min pControl sample. For the one-step phage growth curves (burst time and size), 2 mL samples of the cells resuspended at and OD_{600} of 1.0 in LB + 10 mM $MgSO_4$ + 2 mM $CaCl_2$ (as above) were infected with phage Bas24 at an MOI of 10^{-4}, then the samples were mixed and two 10-fold diluted samples were prepared, then the dilution series for each sample was incubated at 30°C without shaking. At the indicated timepoints, 100 μL samples of each dilution were removed and added to 0.35% LB Agar seeded with ΔRM + pControl (as an indicator lawn), then poured on top of 1.5% LB agar + Cm. All overlay plates were incubated overnight at 30°C before counting plaques. For each timepoint, the plaque forming units (PFU) were normalized to the PFU of the 0 min pControl samples.

Conjugation assays

Plasmids encoding kanamycin (Km) resistance and each possessing different origins of replications (ColE1: pMAT16, RSF1010: pPF1825[39], pBBR1: pSEVA237R[40], or RK2: pPF1619) were conjugated from the *E. coli* donor ST18[41,42] (an auxotroph requiring supplementation with 5-aminolevulinic acid; ALA) into the *E. coli* recipient ΔRM possessing either pControl or p*Ec*ZorI. Mattings were performed at the indicated donor to recipient ratios (D:R) and incubated overnight on LB agar + Cm + ALA at 30°C. The conjugation efficiency was determined by plating dilution series of the matings onto LB agar + Cm + Km (transconjugants) and LB agar + Cm (total recipients). The transconjugant frequency was defined as the transconjugant CFU/recipient CFU.

Transformation assays

Chemically competent cells of ΔRM possessing either pControl or p*Ec*ZorI were prepared by the Inoue method[43], with HEPES-KOH pH 6.8 used for the transformation buffer. Cells were stored in 200 µL aliquots at -80°C prior to use. For each transformation assay, 5 ng of plasmid (quantitated using a Qubit BR kit) was used. Plasmids used were as above for the conjugation assays (ColE1: pMAT16, or pBBR1: pSEVA237R).

Cell survival assays

Overnight cultures of ΔRM possessing either pControl or p*Ec*ZorI were used to inoculate fresh LB + Cm cultures at a 1:100 dilution. The inoculated cultures were grown at 30°C with shaking until reaching an OD_{600} of 0.4–0.6, then harvested by centrifugation, washed with LB + Cm, and resuspended at an OD_{600} of 0.2. Phage Bas24 was then added at an MOI of 5 to each sample; control samples without phage addition were also included. After 20 min adsorption, 10-fold serial dilutions of each sample were plated (100 µL each) on LB + Cm, then incubated overnight at 30°C. The cell survival rate was calculated as [CFU obtained + Bas24]/[CFU obtained without phage addition].

Phages and phage genome purification

Phage primary stocks were prepared using the double-agar method, with near-confluent plaque overlays. The phages were collected by adding SM buffer (100 mM NaCl, 8 mM $MgSO_4$, 50 mM Tris-HCl pH 7.5, 5mM $CaCl_2$) on top of the overly agar and mixed for 4 h at 4°C. The suspension was collected and centrifuged 15 min at 4000 g. High titer phage samples were obtained by

inoculating 1-3 L of LB with a 10^3 dilution of an overnight culture of ΔRM and grown at 37°C to an OD_{600} of 0.3. The bacterial culture was inoculated with the primary stock to an MOI of 0.025 and infection was carried out at 37°C at 90 rpm until a clear lysate was obtained. The lysate was harvested at 4000 g, for 15 min at 4°C. After decanting the supernatant, 1 µg/mL of DNase I and 1 µg/mL of boiled RNase A were added to the cleared lysate. The lysate was gently stirred at 90 rpm for 30 min at room temperature (RT).

Phages were concentrated by polyethylene glycol (PEG) precipitation. NaCl was gradually added to a final concentration of 1 M, followed by gradual addition of 10% PEG 8,000 with continuous stirring at RT until dissolved. After obtaining a clear solution, the lysate was stirred (100 rpm, 30 min; 4°C) and left overnight at 4°C. The lysate was centrifuged (15,000 g, 1 h, 4°C) and the clear supernatant was removed. The precipitate was resuspended in the minimal amount (up to 2 mL) of SM buffer that allowed solubilization. Insoluble materials were removed by adding 20% v/v of chloroform and centrifuged (8,000 g, 10 min). The supernatant was stored at 4°C to be used as phage sample for the following step. The phage was then purified by rate zonal separation using OptiPrep™ Density Gradient Medium (Sigma Aldrich) density gradient ranging from 50 to 10%, diluted in SM media. Phage sample was applied on the top of the gradient and centrifuged (150,000 g, 18 h, 4°C). The phage was extracted, dialyzed against SM buffer and samples were stored at 4°C. The phage genomes were extracted using the Phage DNA isolation kit from Norgen Biotek, aliquoted and stored at -20°C.

Phage genome labeling

Stocks of Bas24 were treated with Pierce Universal Nuclease following the manufacturer's protocol for 1 h at 37°C. To stain the phage genomic DNA, SYTOX Orange (Invitrogen™) stock solution was added to 10 ml of the phage lysate at a concentration of 1:2,000 and incubated overnight at 4°C in the dark. Stained phage particles were subsequently purified by PEG precipitation. PEG 6,000 was added to the lysate to a final concentration of 10% (w/v) and incubated overnight at 4°C to allow for phage aggregation and precipitation. The lysate was centrifuged at 4,000 g for 30 min at 4°C to pellet the phages and the supernatant was carefully discarded without disturbing the phage pellet. The phage pellet was then washed by gently adding a 1 mL SM buffer, centrifuged at 6,000 g for 2 min and used for subsequent time-lapse microscopy experiments.

Protein expression and purification

ZorAB:

The full-length genes of *E. coli* ZorA and ZorB code for 729 and 246 residues, respectively. The tandem gene was PCR amplified from the *E. coli* strain NCTC9026 genome and subcloned into a modified pET vector containing a C-terminal human rhinovirus (HRV) 3C protease cleavage site and a twin-Strep-tag II (resulting in pET11a-ZorA-ZorB-3C-TSII). The plasmids containing the recombinant genes were transfected into *E. coli* C43(DE3) competent cells and the proteins were expressed in LB medium. When the culture OD_{600} reached to 0.6-0.8, the temperature was decreased from 37°C to 24°C, then grown until the OD_{600} reached approximately 0.8-1.0, before 0.5 mM isopropyl β-D-1-thiogalactopyranoside (IPTG) was added for overnight protein induction. The culture was harvested, and the cell pellet was resuspended in buffer A containing 20 mM HEPES-NaOH pH 7.5, 300 mM NaCl supplemented with EDTA-free protease inhibitor (Thermo Fisher Scientific) and lysozyme from chicken white egg (Sigma) to a final concentration of 50 μg/mL and Deoxyribonuclease I from bovine (Sigma) to a final concentration of 30 μg/mL. The mixture was disrupted by high-pressure homogenizer and spun at 185,000 g for 1 h. The pellet containing the membrane was collected and solubilized using buffer B containing 30 mM HEPES-NaOH pH7.5, 300 mM NaCl, 10% glycerol, 2% Lauryl Maltose Neopentyl Glycol (LMNG; Anatrace), supplemented with EDTA-free protease inhibitor at 4°C for 2 h. The solubilized membrane was then spun at 90,000 g for 40 min and the supernatant was loaded onto a gravity flow column containing 2 mL (resin volume) of Strep-Tactin® Superflow® high-capacity resin (IBA), pre-equilibrated with wash buffer containing 20 mM HEPES-NaOH pH 7.5, 300 mM NaCl, 10% glycerol and 0.005% LMNG. The resins were washed five times with 2-3 resin volumes of the wash buffer and elution was carried out five times with 0.5 resin volume (1 mL) of elution buffer containing 20 mM HEPES-NaOH pH 7.5, 300 mM NaCl, 10% glycerol, 0.005% LMNG and 10 mM desthiobiotin). The recombinant protein was then concentrated and loaded onto a pre-equilibrated (20 mM HEPES-NaOH pH 7.5, 150 mM NaCl, 0.002% LMNG) Superose 6 Increase 10/300 GL size exclusion chromatography column. Fractions from the elution peak corresponding to the molecular weight of ZorAB complex were pooled, and the protein was concentrated for cryo-EM grid preparation and functional experiments. The procedures of expression and purification of ZorAB mutants were similar as the ZorAB wild type.

ZorB and MotB soluble peptidoglycan binding domains:

The peptidoglycan binding domains (PGBDs) of each ZorB and $ZorB^{Y151A\text{-}N152A\text{-}L155A\text{-}R159A}$ (from R52 to C-terminus) and *E. coli* MotB (from E96 to C-terminus) were cloned from the existing full-length expression constructs[11] in pET11a by PCR amplification-based deletion mutagenesis (TakaraBio). The ZorB and MotB PGBDs were purified similarly to ZorC and ZorD with a few modifications. The ZorB and the $ZorB^{Y151A/N152A/L155A/R159A}$ PGBD vectors were transformed into Rosetta-gami-2(DE3) competent *E. coli* (Novagen). Cells were grown in LB media supplemented with 100 μg/mL ampicillin, 34 μg/mL chloramphenicol, and 10 μg/mL tetracycline at 37 °C to an $OD600_{nm}$ of 0.7. The cells were then induced with 0.5 mM isopropyl β-D-1-thiogalactopyranoside

(IPTG) and allowed to grow for 16 hours at 18°C. The cultures were harvested and the cell pellets resuspended in lysis/wash buffer (50 mM Tris-HCl pH 8.0, 150 mM NaCl supplemented with EDTA-free protease inhibitor cocktail (Roche). In addition, 1 mg of DNaseI and 0.5 mM $MgCl_2$ was added to the resuspended cells. The cells were lysed using an Avestin Emulsiflex C3 homogeniser, cooled to 4°C, and soluble lysates were cleared by centrifugation at 30 000 g at 4°C for 30 min. The supernatant was then run over a gravity flow column containing 2 mL (resin volume) of Strep-Tactin® 4Flow® high capacity resin (IBA), pre-equilibrated with wash buffer (50 mM Tris-HCl pH 8.0, 150 mM NaCl). The resin was washed with 20 mL lysis/wash buffer and protein was eluted in 12 mL elution buffer (50 mM Tris-HCl pH 8.0, 150 mM NaCl, 10 mM desthiobiotin). The elution was then concentrated and run over a Superose 6 Increase 10/300 GL size exclusion chromatography column into gel filtration buffer (20 mM Tris-HCl pH 8.0, 150 mM NaCl). The MotB PGBD was expressed and purified identically to the ZorB PGBDs, with the exception that it was expressed in BL21(DE3) gold *E. coli*, in LB media supplemented with 100 µg/mL ampicillin.

ZorC:

The predicted ZorC gene codes for 560 residues. The ZorC gene together with a short region upstream of ZorC N-terminus that codes for 7 residues (LPVGYAT) was PCR amplified from the DNA genome of *E. coli* strain NCTC9026 and subcloned into the modified pET vector (resulting in pET11a-ZorC-3C-TSII). *E. coli* BL21 (DE3) gold chemically competent cells were transformed with the plasmids and the protein was expressed in LB medium with the presence of 100 µg/mL of ampicillin. Briefly, when the OD_{600} reached 1.0-1.2, the temperature was decreased to 16°C and 0.5 mM isopropyl β-D-1-thiogalactopyranoside (IPTG) was added for overnight protein induction. The culture was harvested, and the cell pellet was resuspended using buffer containing 20 mM Tris-HCl pH 7.5, 10% glycerol and 500 mM NaCl supplemented with EDTA-free protease inhibitor (Thermo Fisher Scientific). The cells were lysed using an Avestin Emulsiflex C3 homogeniser, cooled to 4°C, and spun at 18,000 g for 40 min. The supernatant was then added to a gravity flow column containing 3 mL (resin volume) of Strep-Tactin® Superflow® high-capacity resins (IBA), pre-equilibrated with wash buffer (20 mM Tris-HCl pH 7.5, 10% glycerol and 500 mM NaCl). Resins were washed five times with 2-3 resin volumes of wash buffer and elution was performed with 4 CV of elution buffer (20 mM Tris-HCl pH 7.5, 500 mM NaCl and 10 mM desthiobiotin). The recombinant protein was pooled and concentrated and was loaded onto a pre-equilibrated (20 mM Tris-HCl pH 7.5, 500 mM NaCl) Superose 6 Increase 10/300 GL size exclusion chromatography column. Peak fractions were pooled, and another round of size exclusion chromatography was carried out with buffer 20 mM HEPES-NaOH pH 7.5, and 150 mM NaCl to decrease NaCl concentration. Fractions from the elution peak corresponding to the molecular weight of ZorC were pooled and the protein was concentrated to approximately 1 mg/mL for cryo-EM grids preparation and functional experiments. ZorC proteins used for electromobility shift assays (EMSAs) were exchanged into buffer containing 20 mM Tris-HCl pH 7.5, 300 mM NaCl, 10% glycerol, 1 mM TCEP following elution. Pure fractions were concentrated

and flash frozen in small aliquots and stored at -80°C until use. Sample purity was assessed by SDS-PAGE. The procedures of expression and purification of ZorC mutants were similar to those for the ZorC wild type.

ZorD:

The predicted ZorD gene coding 1,086 residues was PCR amplified from the DNA genome of *E. coli* strain NCTC9026 and was subcloned into the modified pET vector, resulting in pET11a-ZorC-3C-TSII. The expression and purification of ZorD protein were similar to ZorC protein, except for the purification buffer. Briefly, the suspension buffer contained 150 mM NaCl, 20 mM HEPES-NaOH pH 7.5, and 10% glycerol; the wash buffer was the same as the suspension buffer and the elution buffer contained 150 mM NaCl, 20 mM HEPES-NaOH pH 7.5, 10% glycerol, and 10 mM desthiobiotin; and the size exclusion chromatographic buffer contained 150 mM NaCl and 20 mM HEPES-NaOH pH 7.5. Purified ZorD was concentrated to 0.4-0.6 mg/mL for functional experiments and cryo-EM grid preparation. For nuclease experiment, ZorD protein was kept in the elution buffer and flash frozen in small aliquots and stored at -80°C until use.

Cryo-EM grid preparation, data collection, model building, and refinement.

ZorAB:

Freshly purified ZorAB sample was concentrated to 2-3 mg/mL and 2.7 μL protein was applied onto glow-discharged (30 s, 5 mA) grids (Quantifoil R0.6/1 300 mesh Au) and plunge-frozen into liquid ethane using a Vitrobot Mark IV (FEI, Thermo Fisher Scientific), with the settings: 100% humidity, 4ºC, blotting force 25, 4-6 s blot time and 7 s wait time. Movies were collected using the semi-automated acquisition program EPU (FEI, Thermo Fisher Scientific) on a Titan Krios G2 microscope operated at 300 keV paired with a Falcon 3EC direct electron detector (FEI, Thermo Fisher Scientific). Images were recorded in electron counting mode, at 96,000x magnification with a calibrated pixel size of 0.832 Å and an underfocus range of 0.7 to 2.5 μm. The number of micrographs and total exposure values for the different datasets are summarized in Table S1. Grid preparation, and data collection strategies of the ZorAB mutants were similar to those for the ZorAB wild type.

ZorC:

Purified ZorC (3 μL at ~1 mg/mL) was applied onto glow-discharged (30 s, 5 mA) grids (UltrAuFoil R 0.6/1, 300 mesh, Gold) and plunge-frozen into liquid ethane using a Vitrobot Mark IV (FEI, Thermo Fisher Scientific), with the settings: 100% humidity, 4 ºC, blotting force 20, 4 s blot time and 10 s wait time. Movies were collected using the semi-automated acquisition program EPU (FEI, Thermo Fisher Scientific) on a Titan Krios G2 microscope operated at 300 keV paired with a Falcon 3EC direct electron detector (FEI, Thermo Fisher Scientific). Images were recorded in electron counting mode, at 96,000x magnification with a calibrated pixel size of 0.832 Å and an underfocus range of 1 to 2.5 μm. The number of micrographs and total exposure values for the

datasets are summarized in **Extended Data Table 1**. For the ZorC + DNA sample, ZorC (final concentration 0.6 mg/mL) was mixed with commercial pUC19 plasmid (NEB) (final concentration of 0.5 μg/μl). Samples were incubated at room temperature for 30 min, followed by 30 min at 4ºC prior to grid preparation. Samples (3 μL) were applied to UltraAuFoil R 2/2, 200 mesh Gold grids (glow discharged 60 s at 10 mA) and plunge-frozen as above, but with the settings: blotting force 15, and 3 s blot time.

ZorD:
ZorD showed preferred orientation of particles on ice. Zwitterionic detergent (0.5% CHAPSO; Anatrace) was added to the purified sample to a final concentration of 0.0125% before cryo-EM grid preparation. For the apo form, the preparation of grids was similar to ZorC. For ZorD in complex with ATP-γ-S, 4 μL of 0.1 mM ATP-γ-S was added into 400 μL of purified ZorD at 0.0375 mg/ml. The mixture was concentrated to 15 μL to reach a ZorD concentration of around 0.6 mg/mL. The grid preparation was similar to ZorC. The number of micrographs and total exposure values for the different datasets are summarized in **Extended Data Table 1**.

Cryo-EM data processing

All datasets were processed using cryoSPARC[44] v4.2.1, unless otherwise stated. We started by using Patch motion correction to estimate and correct for full-frame motion and sample deformation (local motion). Patch Contrast function (CTF) estimation was used to fit local CTF to micrographs. Micrographs were manually curated to remove low-quality data (the relative ice thickness value greater than 1.1 and the CTF value worse than 3.5 Å). We performed particle picking by template picking or using topaz particle picking[45]. Particles were extracted with a box size of 500 pixels for ZorAB datasets, 256 pixels for the ZorC dataset, and 400 pixels for the ZorD dataset. One round of 2D classification was performed followed by *ab initio* reconstruction. Heterogeneous refinement was used to exclude broken particles. Non-uniform refinement was applied with a dynamic mask to obtain a high-resolution map. Local refinement was additionally performed with a soft mask to achieve a higher-resolution map of some flexible regions. For all datasets, the number of movies, the number of particles used for the final refinement, map resolution, and other values during data processing are summarized in the **Extended Data Table 1**.

Model building and validation

We used AlphaFold2 or AlphaFold3[24] to predict all the initial models. The predicted models were manually fit into the cryo-EM density by using UCSF ChimeraX[46]. The model was refined in Coot[47] or using StarMap[48] in the case of ZorC, for which the map is anisotropic and the resolution is modest. The model was then refined against the map using PHENIX real space refinement[49].

The ZorAB composite model was constructed by extending the pentameric tail as an idealized right-handed super-helical coiled coil. Local conformations were manually adjusted in PyMol[50](v2.5) and optimized through energy minimization using GROMACS (v2022.5)[51] with CHARMM27 force field. However, it is worth noting an irregularity in the AF2 model, specifically in residues 312 to 322, which introduces a substantial twist in the ZorA tail, raising possibilities of other pentameric forms of the ZorA tail and further reflecting its conformational dynamics.

Peptidoglycan (PG) purification and pull-down experiments

Peptidoglycan was purified from *E. coli* ΔRM with the protocol adapted from[52]. Briefly, ΔRM cells were incubated in 1 L LB media until the OD_{600} reached 0.8. Cells were harvested and resuspended in 12 mL PBS buffer and split into two 50 mL Falcon tubes, then 10% w/v SDS solution (in PBS) was added to a final concentration of 6% w/v. The Falcon tubes were boiled for 1 hour while stirred at 500 rpm. The heat was turned off and the tube was allowed to cool to ambient temperature overnight. The next day, the solutions from both Falcon tubes were pooled into one 50 mL Falcon tube, and centrifuged at room temperature for 45 mins at 108,000 g. The pellet was washed five times with 5 mL Milli-Q water. The PG was resuspended in 20 mL of buffer containing 50 mM Tris-HCl pH 7.0, and α-amylase was added (SigmaAldrich) to a final concentration of 100 µg/mL and incubated for 2 hours at 37°C. Next, 50 µg/mL RNase A (Roche) and 10 µg/mL DNase (Sigma-Aldrich) were added and incubated for an additional 2 hours at 37°C. Then, the mixture was supplemented with 20 mM $MgSO_4$, 10 mM $CaCl_2$, and 100 µg/mL trypsin (SigmaAldrich), and incubated at 37°C overnight. The following day, EDTA at pH 8 was added to a final concentration of 10 mM and 10% w/v SDS solution to a final concentration of 1% w/v. The mixture was boiled for 20 mins in a water bath and allowed to cool to ambient temperature. The tube was centrifuged at 108,000 g for 45 min. The resulting pellet was washed five times with Milli-Q water to remove residual SDS. Finally, the pellet was resuspended in 300 µL of Milli-Q water, aliquoted into 35 µL portions, and stored at -20°C. For PG pull-down assays, the purified PG was washed with 1 mL PBS + 0.002% LMNG buffer and centrifuged at 20,000 g for 30 min. Purified ZorAB and ZorAB $ZorB^{Y151A/N152A/L155A/R159A}$ mutant (10 µL, at a concentration of 2 mg/mL; ZorAB $ZorB^{Y151A/N152A/L155A/R159A}$ mutant is less stable, requiring using freshly purified protein) was incubated with the PG at room temperature for 1 hour, then centrifuged at 20,000 g for 30 min. The pellet was washed 3 times with 700 µL of the pull-down buffer by mixing and centrifugation (10 min, 12°C, 20,000 g). The supernatant was retained for SDS gel analysis. The pellet was resuspended with 20 µL of buffer and 5 µL of loading dye was added for SDS gel analysis.

For the pull downs of ZorB PGBD, mutant ZorB PGBD ($ZorB^{Y151A/N152A/L155A/R159A}$ PGBD), MotB PGBD (positive control) and ZorE (negative control), the protocol was similar as above. Briefly, PG (PGN-ECndi ultrapure peptidoglycan (InvivoGen); due to the low yield of the lab-purified PG), was washed and resuspended in resuspension buffer (20 mM potassium phosphate pH 7, 150 mM NaCl). Each pull-down reaction contained 10 µL of washed 25 mg/mL PG, 4 µL of the

indicated protein (each added from a 5 mg/mL stock) and the pull-down buffer (20 mM potassium phosphate pH 6, 150 mM NaCl, 2 mM $MgCl_2$, 2 mM $CaCl_2$) to final volume of 100 µL. The samples were incubated for 30 min at 20°C, mixing gently. The insoluble PG was pelleted by centrifugation at 20,000 g, at 12°C for 10 minutes and the soluble supernatant was retained for SDS-PAGE analysis. The pellet was washed 3 times with 700 µL of the pull-down buffer by mixing and centrifugation (10 min, 12°C, 20,000 g). Finally, the pellet was resuspended in 100 µL of pull-down buffer and 15 µL of each sample (soluble supernatant and resuspended pellet) was mixed with 3 µL loading dye for SDS-PAGE analysis.

ZorC DNA-binding experiments

Electromobility shift assays:

Frozen aliquots of ZorC and ZorC mutants in ZorC buffer (20 mM Tris-HCL pH 7.5, 300 mM NaCl, 10% glycerol, 1 mM TCEP) were thawed and centrifuged to remove possible aggregates. ZorC was diluted to 10x stocks for each concentration used, in the same ZorC buffer. The final EMSA reaction buffer contained phosphate-buffered saline (15.2 mM $NaHPO_4$, 0.90 mM $CaCl_2$, 2.7 mM KCl, 1.47 mM KH_2PO_4, 8.1 mM Na_2HPO_4, 0.49 mM $MgCl_2$, 137.9 mM NaCl) at pH 7.4 and 10% glycerol. ZorC or ZorC buffer was then added, followed by DNA substrate (10x stock in H_2O) or H_2O. DNA oligos with 5'-FAM modifications were synthesized by TAG Copenhagen A/S and double strand constructs were obtained by annealing the unlabeled complement sequence (The dsDNA sequences used in this study is shown in **Extended Data Fig. 7h**). All components were incubated at 4°C for 30 min and loaded on a 1.5% w/v agarose gel made with 20 mM sodium phosphate buffer (pH 7.2). Samples were run for 30 min at 100V, at 4°C using 20 mM sodium phosphate (pH 7.2) as running buffer. The gels were visualized using Odyssey® XF Imaging System at 600 nm.

Nuclease assays

ZorD was incubated with 200 ng pUC19 (linearized by KpnI) in the reaction buffer containing 1 × Cutsmart buffer (NEB), 2 mM ATP (NEB) in a total volume of 25 µl. The reactions were incubated at 37°C for 1 hour with shaking at 600 rpm using an Eppendorf ThermoMixer. DNA product was purified using a NucleoSpin Gel and PCR Clean-up kit (Machery Nagel) using the standard protocol and was analyzed with 1% E-Gel™ EX. For the reaction with the phage genomes, 200 nM Proteins were incubated with around 100 ng purified phage genomic DNA in the same reaction buffer indicated above. The reactions were terminated by adding 1× E-gel loading buffer and product was analyzed with 1% E-Gel™ EX.

Mass spectrometry sample preparation

Overnight cultures of *E. coli* ΔRM transformed with p*Ec*ZorI (or pControl), were used to inoculate (at a 1:1000 dilution) 3 mL LB media with antibiotics, then grown to an OD_{600} of approximately 0.4. The cell pellet was collected, resuspended in 500 µL of 0.2 M Tris-HCl pH 8.0, and incubated for 20 min. Next, 250 µL of buffer (0.2M Tris-HCl pH 8.0, 1 M sucrose, and 1 mM EDTA) was added, along with 3 µL of 10 mg/mL lysozyme. The mixture was incubated for 30 min, and 250 µL of 6% w/v SDS was added to a final concentration of 1%, after which the sample was heated at 99°C for 10 min. The mixture was sonicated (Misonix Ultrasonic Liquid Processor with microtip Probe) to fragment DNA and RNA with the settings: amplitude 10, time 5 s sonication and 5 s pause and 5 cycles.

For mass spectrometry (MS analysis), we performed Protein Aggregate Capture digestion of proteins[53]. To this end, 250 µL of bacterial lysate was taken from the total sample, and 750 µL of acetonitrile was added into the mixture, along with 50 µL magnetic microspheres that had been prewashed with PBS buffer. The mixture was allowed to settle for 10 min, prior to retention of the magnetic microspheres by magnetic plate. Beads were washed once with 1 mL acetonitrile, and once with 1 mL of 70% ethanol, after which all ethanol was removed and the beads were stored at −20°C until further processing. Frozen beads were thawed on ice, supplemented with 100 µL ice-cold 50 mM Tris-HCl pH 8.5 buffer supplemented with 2.5 ng/µL Lys-C, and gently mixed (on ice) every 5 min for 30 min. Digestion was performed for 3 h using a Eppendorf ThermoMixer shaking at 1,250 rpm at 37°C. Following this, beads were chilled on ice, and 250 ng of sequencing-grade trypsin was added, after which samples were gently mixed (on ice) every 5 min for 30 min. Final digestion was performed overnight using a Eppendorf ThermoMixer shaking at 1,250 rpm at 37°C. Peptides were separated from magnetic microspheres using 0.45 µm filter spin columns, and peptides were reduced and alkylated by adding TCEP and chloroacetamide to 5 mM for 30 min prior to peptide clean-up via low-pH C18 StageTip procedure. C18 StageTips were prepared in-house, by layering four plugs of C18 material (Sigma-Aldrich, Empore SPE Disks, C18, 47 mm) per StageTip. Activation of StageTips was performed with 100 µL 100% methanol, followed by equilibration using 100 µL 80% acetonitrile (ACN) in 0.1% formic acid, and two washes with 100 µL 0.1% formic acid. Samples were acidified to pH <3 by addition of trifluoroacetic acid to a concentration of 1%, after which they were loaded on StageTips. Subsequently, StageTips were washed twice using 100 µL 0.1% formic acid, after which peptides were eluted using 80 µL 30% ACN in 0.1% formic acid. All fractions were dried to completion using a SpeedVac at 60°C. Dried peptides were dissolved in 25 µL 0.1% formic acid (FA) and stored at −20°C until MS analysis.

Approximately 1 µg of peptide was analyzed per injection. All samples were analyzed on an EASY-nLC 1200 system (Thermo Fisher Scientific) coupled to an Orbitrap™ Astral™ mass

spectrometer (Thermo Fisher Scientific). Samples were analyzed on 20 cm long analytical columns, with an internal diameter of 75 µm, and packed in-house using ReproSil-Pur 120 C18-AQ 1.9 µm beads (Dr. Maisch). The analytical column was heated to 40°C, and elution of peptides from the column was achieved by application of gradients with stationary phase Buffer A (0.1% FA) and increasing amounts of mobile phase Buffer B (80% ACN in 0.1% FA). The primary analytical gradient ranged from 10 %B to 38 %B over 57.5 min, followed by a further increase to 48 %B over 5 min to elute any remaining peptides, and by a washing block of 15 min. Ionization was achieved using a NanoSpray Flex NG ion source (Thermo Fisher Scientific), with spray voltage set at 2 kV, ion transfer tube temperature to 275°C, and RF funnel level to 50%. All full precursor (MS1) scans were acquired using the Orbitrap™ mass analyzer, while all tandem fragment (MS2) scans acquired in parallel using the Astral™ mass analyzer. Full scan range was set to 300-1,300 m/z, MS1 resolution to 120,000, MS1 AGC target to "250" (2,500,000 charges), and MS1 maximum injection time to "150". Precursors were analyzed in data-dependent acquisition (DDA) mode, with charges 2-6 selected for fragmentation using an isolation width of 1.3 m/z and fragmented using higher-energy collision disassociation (HCD) with normalized collision energy of 25. Monoisotopic Precursor Selection (MIPS) was enabled in "Peptide" mode. Repeated sequencing of precursors was minimized by setting expected peak width to 20 s, and dynamic exclusion duration to 20 s, with an exclusion mass tolerance of 10 ppm and exclusion of isotopes. MS2 scans were acquired using the Astral mass analyzer. MS2 fragment scan range was set to 100-1,500 m/z, MS2 AGC target to "50" (5,000 charges), MS2 intensity threshold to 50,000 charges per second, and MS2 maximum injection time to 5 ms; thus requiring a minimum of 250 charges for attempted isolation and identification of each precursor. Duty cycle was fixed at 0.3 s, acquiring full MS scans at ~3.3 Hz and with auto-fitting of Astral scans resulting in MS2 acquisition at a rate of ~100-200 Hz.

Mass spectrometry data analysis

All RAW files were analyzed using MaxQuant software (v2.4.3.0)[54], the earliest release version to support Astral RAW files. Default MaxQuant settings were used, with exceptions outlined below. For generation of the in silico spectral library, the four full-length Zorya protein sequences were entered into a FASTA database, along with all (23,259) Swiss-Prot-reviewed *E. coli* sequences (taxonomy identifier 562) downloaded from UniProt[55] on the 7th of September, 2023. The data was first searched using pFind (v3.2.0)[56], using the "Open Search" feature to determine overall peptide properties and commonly occurring (affecting >1% of PSMs) peptide modification in an unbiased manner. For searching Astral .RAW files using pFind, .RAW files were first converted to .mzML using OpenMS (v3.0.0)[57]. For the main data search using MaxQuant, digestion was performed using "Trypsin/P" with up to 2 missed cleavages (default), with a minimum peptide length of 6 and a maximum peptide mass of 5,000 Da. No variable modifications were considered for the first MS/MS search, which is only used for precursor mass recalibration.

For the MS/MS main search a maximum allowance of 3 variable modifications per peptide was set, including protein N-terminal acetylation (default), oxidation of methionine (default), deamidation of asparagine, peptide N-terminal glutamine to pyroglutamate, and replacement of three protons by iron (cation Fe[III]) on aspartate and glutamate. Unmodified and modified peptides were stringently filtered by setting a minimum score of 10 and 20, and a minimum delta score of 20 and 40, respectively. First search mass tolerance was set to 10 ppm, and maximum charge state of considered precursors to 6. Label-free quantification (LFQ) was enabled, "Fast LFQ" was disabled. iBAQ was enabled. Matching between runs was enabled with a match time window of 1 min and an alignment time window of 20 min. Matching was only allowed between same-condition replicates. Data was filtered by posterior error probability to achieve a false discovery rate of <1% (default), at the peptide-spectrum match, protein assignment, and site-decoy levels.

Mass spectrometry data statistics

All statistical data handling was performed using the Perseus software[58], including data filtering, log2-transformation, imputation of missing values (down shift 1.8 and width 0.15), and two-tailed two-sample Student's t-testing with permutation-based false discovery rate control. In order to determine relative concentration of all proteins in the samples, LFQ-normalized intensity values for each protein were adjusted by molecular weight. To approximate absolute copy numbers, we extracted known protein copy numbers based on the "LB" condition as reported by Schmidt et al.,[59] log2-transformed them, and aligned them to the molecular-weight adjusted LFQ intensity values from our own data, resulting in 1,901 out of 2,418 quantified protein-groups receiving a known copy number value ($R^2 = 0.6129$). Next, we subtracted the overall median from all log2 values and determined the absolute delta between the values of each pair. Out of all pairs, 459 had a log2 delta of <0.5, which we considered as a "proteomic ruler". Linear regression was performed on the remaining pairs ($R^2 = 0.9868$) to determine a conversion factor between MW-adjusted LFQ intensity and absolute copy number.

TIRF microscopy cultivation conditions

Overnight cultures of *E. coli* strains expressing ZorB-HaloTag, ZorC or ZorD translational fusions to mNeongreen (mNG) were incubated shaking at 180 rpm in LB Lennox containing 20 mM $MgSO_4$, 5 mM $CaCl_2$ and supplemented with 12.5 µg/ml Cm at 30°C. On the next day, a sub-culture was inoculated 1:100 and grown at 30°C until an OD_{600} between 0.3-0.5 was reached. Subsequently, cells were diluted to an OD_{600} of 0.2. For HaloTag fusions, cells were washed once in PBS supplemented with a final concentration of 0.2% glucose and stained with 1 µM TMR ligand for 30 min. To remove excess of TMR following staining, cells were washed twice with PBS supplemented with 0.2% glucose. Cells were then exposed to phages at indicated MOIs or

incubated untreated for 30 min in a 2 mL Eppendorf tube under shaking conditions (<650 rpm in an Eppendorf ThermoMixer) at 30°C. For TIRF microscopy, 1 µl of cells and phage mix was spotted on an agarose pad (1.2% in MQ of UltraPure™ Agarose, Invitrogen) and directly imaged.

TIRF microscopy acquisition and data evaluation

TIRF microscopy was performed using a Nikon Eclipse Ti2 inverted microscope equipped with an ILAS 2 TIRF module (Gataca Systems) and a TIRF 100x/1.49 oil objective. Samples were excited at 50 ms exposure for 14 frames using a 488 nm laser (power of 550 µW with a sensor area of 283.5 mm^2) at 80% and emission was recovered via a quad TIRF filter cube (emission: 502-549 nm). For the HaloTag constructs, 5 frames were acquired using a 561 nm laser (power of 930 µW with a sensor area of 283.5 mm^2) at 80% with an exposure time of 50 ms. Emission was recovered via a quad TIRF filter cube (emission: 581-625 nm, followed by an emission wheel filter: 580-611 nm). The second frame (for HaloTag constructs the third frame) in the fluorescent channel of the acquired TIRF microscopy images was denoised using the Nikon software package Denoise.ai. Subsequently, fluorescent maxima of ZorB, ZorC or ZorD translational fusions to mNG were detected using MicrobeJ[60] run in Fiji[61]. For the co-localization analysis of ZorB-HT with either ZorC-mNG or ZorD-mNG, ZorB foci detection was performed using ilastik[62]. Subsequently, the obtained ZorB binary masks were overlayed in MicrobeJ onto the original image and cells were manually detected in MicrobeJ. From this, parameters such as ZorB foci count, intensity in both HaloTag and mNG channel per cell and mNG signal of the entire cell body were extracted. We defined co-localization of ZorB with a cytoplasmic Zorya component (ZorC or ZorD) if mNG signal within the detected ZorB complex area was 1.5x fold greater than the average cytoplasmic mNG fluorescence of the complete cell. Finally, cells containing at least one ZorB with either ZorD or ZorC were considered as co-localized. Statistics were calculated in Prism GraphPad 9 by applying the in-built analyses of unpaired t-tests or one-way ANOVA.

Time-lapse microscopy and data evaluation

Cells were prepared as stated above for TIRF microscopy. In case of the Bas54-*parS* phage infection experiments, the *E. coli* cells expressed an IPTG-inducible $ParB^{P1}$-mScarlet fusion protein from pALA2703-mScarlet-$ParB^{P1}$ in addition to EcZorI or the empty vector control[63]. After diluting the sub-culture to an OD_{600} of 0.2, cells were exposed to phages at an MOI of 5 (or unknown if labeled) for 5 min (or none) under shaking conditions and subsequently 1 µl was spotted onto a 1.2% w/v agarose pad (dissolved in LB:MQ with a ratio of 1:5). Expression of $ParB^{P1}$-mScarlet was induced by addition of 500µM IPTG in the sub-culture. For the time-lapse experiments involving CCCP, cells were exposed to 30 µM CCCP and Bas24 MOI of 5 for 30 min (or CCCP only) under shaking conditions and followed by spotting 1 µl onto an agarose pad (composition as above, supplemented with 30 µM CCCP). Microscopy slides were then mounted

into a preheated to 37 °C incubation chamber surrounding the microscope. Acquisition was performed using a Nikon Eclipse Ti2 inverted microscope equipped with a CFI Plan Apochromat DM 60x Lambda oil Ph3/1.40 objective and phase contrast images were obtained every two minutes for the indicated time span. Obtained time-lapse images were segmented using ilastik to detect the cell areas[61]. Time-lapse microscopy movies of DNA-labeled Bas24 and Bas54-*parS* phage infection experiments were x,y drift corrected using the Fiji Fast4DReg plugin[64,65]. The intensity decay due to photobleaching of the SYTOX Orange fluorescent channel was subsequently corrected using the Bleach Corrector Fiji plugin[66]. Final graphs and movies were prepared using a custom Python script.

Construction of the phage Bas54-parS

A *parS* site was introduced between gp69 and gp70 of phage MaxBurger (Bas54)[15] by homologous recombination with a synthetic template followed by CRISPR-Cas13a selection against the parental wildtype using a setup similar to the procedure described elsewhere[67]. In a first step, the *parS* sequence (TCGCCATTCAAATTTCACTATTAACTGACTGTTTTTAAA GTAAATTACTCTAAAATTTCAAGGTGAAATCGCCACGATTTCAC) was inserted between plasmid-encoded homology arms of 100-200 bp length by PCR[68], creating pAH210_Bas54_parS_H1. Subsequently, an *E. coli* K-12 host was transformed with this plasmid and then infected with phage Bas54 to enable homologous recombination. The lysate from this infection – containing wildtype and recombinant phages – was then subjected to CRISPR-Cas13a selection against the parental wildtype using a crRNA targeting CTCTGAAGACCTCCAGTAGTAAGATGTAAGT (5'-3') which includes the 3' end of gp69 and the downstream region which is disrupted by insertion of the *parS* site. CRISPR-Cas13a selection was performed using a two-plasmid setup of pAH221 (expressing LbuCas13a) and pAH218_LbuCas13a_parS_H1 (expressing the crRNA). Plaques growing after CRISPR-Cas13a selection were screened for successful insertion of the *parS* site by PCR and the sequence of the recombinant was confirmed by Sanger sequencing.

Bioinformatic analyses of ZorA motor and tail lengths

PADLOC v1.1.0[32] with PADLOC-DB v1.4.0 was used to identify Zorya systems in RefSeq v209[33] bacterial and archaeal genomes. Of the systems identified, we excluded those containing pseudogenes or more than one copy of each Zorya gene, or systems with non-canonical gene arrangements (Zorya genes are typically on the same strand, in type-specific conserved gene orders, e.g. *zorABCD*, *zorABE*, or *zorGABF* for types I–III, respectively). To reduce redundancy due to highly related genome sequences in the RefSeq database, we then selected representative Zorya systems by first clustering the sequences (using MMseqs2 v14.7e284[34] with options: --min-

seq-id 0.3 --coverage 0.8) of the proteins encoded by the three adjacent open reading frames on either side of each Zorya system, then randomly selecting one representative system for each unique genetic context observed. The ZorA and ZorB sequences from the representative Zorya systems were then clustered using MMseqs2 with options: --min-seq-id 0.3 --coverage 0.95. Structures were predicted for each MMseqs2 cluster representative of each ZorA and ZorB family using ColabFold v1.5.2[69] with options: --num-recycle 3 --num-models 1 --model-type auto --amber --use-gpu-relax. Structure predictions were run as $ZorA_5ZorB_2$ multimers. The resulting structures were inspected manually (using PyMOL v2.5.4[50]) to identify the start of the ZorA tail. The rest of the sequences in each cluster were aligned to the representative sequence using MUSCLE v5.1[35] using the Parallel Perturbed ProbCons algorithm (default) or the Super5 algorithm if the cluster contained more than 100 sequences. The start of the tail for the representative was used to infer the start of the tail for each other protein in the respective alignment.

Figure preparation

Structural figures were prepared using ChimeraX version 1.8[46], PyMOL version 2.5.4 and 3.0.2[50], Prism GraphPad9 or GraphPad Prisim10[70] and Adobe Illustrator[71]. The ion permeation pathway shown in ZorAB was analyzed using MOLEonline[72]. The Hydrophobicity and polarity of the ZorAB tail was calculated using MOLEonline[72]. The electrostatic potential maps were calculated using the APBS[73] electrostatic Plugin integrated inside PyMOL. Full gel/blot images for all relevant figures are provided in **Supplementary Figure 1**.

Additional References:

32. Payne, L. J. *et al.* PADLOC: a web server for the identification of antiviral defence systems in microbial genomes. *Nucleic Acids Res.* **50**, W541–W550 (2022).

33. Haft, D. H. *et al.* RefSeq: an update on prokaryotic genome annotation and curation. *Nucleic Acids Res.* **46**, D851–D860 (2018).

34. Steinegger, M. & Söding, J. MMseqs2 enables sensitive protein sequence searching for the analysis of massive data sets. *Nat. Biotechnol.* **35**, 1026–1028 (2017).

35. Edgar, R. C. Muscle5: High-accuracy alignment ensembles enable unbiased assessments of sequence homology and phylogeny. *Nat. Commun.* **13**, 6968 (2022).

36. Price, M. N., Dehal, P. S. & Arkin, A. P. FastTree 2 – Approximately Maximum-Likelihood Trees for Large Alignments. *PLOS ONE* **5**, e9490 (2010).

37. Parks, D. H. *et al.* GTDB: an ongoing census of bacterial and archaeal diversity through a phylogenetically consistent, rank normalized and complete genome-based taxonomy. *Nucleic Acids Res.* **50**, D785–D794 (2022).

38. Kim, D., Park, S. & Chun, J. Introducing EzAAI: a pipeline for high throughput calculations of prokaryotic average amino acid identity. *J. Microbiol. Seoul Korea* **59**, 476–480 (2021).

39. McBride, T. M. *et al.* Diverse CRISPR-Cas Complexes Require Independent Translation of Small and Large Subunits from a Single Gene. *Mol. Cell* **80**, 971-979.e7 (2020).

40. Martínez-García, E. *et al.* SEVA 4.0: an update of the Standard European Vector Architecture database for advanced analysis and programming of bacterial phenotypes. *Nucleic Acids Res.* **51**, D1558–D1567 (2023).

41. Thoma, S. & Schobert, M. An improved Escherichia coli donor strain for diparental mating. *FEMS Microbiol. Lett.* **294**, 127–132 (2009).

42. Jackson, S. A., Fellows, B. J. & Fineran, P. C. Complete Genome Sequences of the Escherichia coli Donor Strains ST18 and MFDpir. *Microbiol. Resour. Announc.* **9**, 10.1128/mra.01014-20 (2020).

43. Inoue, H., Nojima, H. & Okayama, H. High efficiency transformation of Escherichia coli with plasmids. *Gene* **96**, 23–28 (1990).

44. Punjani, A., Rubinstein, J. L., Fleet, D. J. & Brubaker, M. A. cryoSPARC: algorithms for rapid unsupervised cryo-EM structure determination. *Nat. Methods* **14**, 290–296 (2017).

45. Bepler, T. *et al.* Positive-unlabeled convolutional neural networks for particle picking in cryo-electron micrographs. *Nat. Methods* **16**, 1153–1160 (2019).

46. Pettersen, E. F. *et al.* UCSF ChimeraX: Structure visualization for researchers, educators, and developers. *Protein Sci. Publ. Protein Soc.* **30**, 70–82 (2021).

47. Emsley, P. & Cowtan, K. Coot: model-building tools for molecular graphics. *Acta Crystallogr. D Biol. Crystallogr.* **60**, 2126–2132 (2004).

48. Lugmayr, W. *et al.* StarMap: a user-friendly workflow for Rosetta-driven molecular structure refinement. *Nat. Protoc.* **18**, 239–264 (2023).

49. Liebschner, D. *et al.* Macromolecular structure determination using X-rays, neutrons and electrons: recent developments in Phenix. *Acta Crystallogr. Sect. Struct. Biol.* **75**, 861–877 (2019).

50. The PyMOL Molecular Graphics System, Version 2.5 Schrödinger, LLC. https://pymol.org/2/support.html?#citing.

51. Abraham, M. J. *et al.* GROMACS: High performance molecular simulations through multi-level parallelism from laptops to supercomputers. *SoftwareX* **1–2**, 19–25 (2015).

52. Kirchweger, P. *et al.* Structural and functional characterization of SiiA, an auxiliary protein from the SPI4-encoded type 1 secretion system from Salmonella enterica. *Mol. Microbiol.* **112**, 1403–1422 (2019).

53. Batth, T. S. *et al.* Protein Aggregation Capture on Microparticles Enables Multipurpose Proteomics Sample Preparation*. *Mol. Cell. Proteomics* **18**, 1027–1035 (2019).

54. Cox, J. & Mann, M. MaxQuant enables high peptide identification rates, individualized p.p.b.-range mass accuracies and proteome-wide protein quantification. *Nat. Biotechnol.* **26**, 1367–1372 (2008).

55. The UniProt Consortium. UniProt: the Universal Protein Knowledgebase in 2023. *Nucleic Acids Res.* **51**, D523–D531 (2023).

56. Chi, H. *et al.* Comprehensive identification of peptides in tandem mass spectra using an efficient open search engine. *Nat. Biotechnol.* (2018) doi:10.1038/nbt.4236.

57. Röst, H. L. *et al.* OpenMS: a flexible open-source software platform for mass spectrometry data analysis. *Nat. Methods* **13**, 741–748 (2016).

58. Tyanova, S. *et al.* The Perseus computational platform for comprehensive analysis of (prote)omics data. *Nat. Methods* **13**, 731–740 (2016).

59. Schmidt, A. *et al.* The quantitative and condition-dependent Escherichia coli proteome. *Nat. Biotechnol.* **34**, 104–110 (2016).

60. Ducret, A., Quardokus, E. M. & Brun, Y. V. MicrobeJ, a tool for high throughput bacterial cell detection and quantitative analysis. *Nat. Microbiol.* **1**, 1–7 (2016).

61. Schindelin, J. *et al.* Fiji - an Open Source platform for biological image analysis. *Nat. Methods* **9**, 10.1038/nmeth.2019 (2012).

62. Berg, S. *et al.* ilastik: interactive machine learning for (bio)image analysis. *Nat. Methods* **16**, 1226–1232 (2019).

63. Li, Y. & Austin, S. The P1 plasmid is segregated to daughter cells by a 'capture and ejection' mechanism coordinated with Escherichia coli cell division. *Mol. Microbiol.* **46**, 63–74 (2002).

64. Laine, R. F. *et al.* NanoJ: a high-performance open-source super-resolution microscopy toolbox. *J. Phys. Appl. Phys.* **52**, 163001 (2019).

65. Jw, P. *et al.* Fast4DReg - fast registration of 4D microscopy datasets. *J. Cell Sci.* **136**, (2023).

66. K, M. Bleach correction ImageJ plugin for compensating the photobleaching of time-lapse sequences. *F1000Research* **9**, (2020).

67. Adler, B. A. *et al.* Broad-spectrum CRISPR-Cas13a enables efficient phage genome editing. *Nat. Microbiol.* **7**, 1967–1979 (2022).

68. Liu, H. & Naismith, J. H. An efficient one-step site-directed deletion, insertion, single and multiple-site plasmid mutagenesis protocol. *BMC Biotechnol.* **8**, 91 (2008).

69. Mirdita, M. *et al.* ColabFold: making protein folding accessible to all. *Nat. Methods* **19**, 679–682 (2022).

70. One-way ANOVA followed by Dunnett's multiple comparisons test was performed using GraphPad Prism version 9.0.0 for Mac OS X, GraphPad Software, Boston, Massachusetts USA, www.graphpad.com.

71. Adobe Illustrator. *PCMag UK* https://uk.pcmag.com/illustration/9711/adobe-illustrator (2021).

72. Pravda, L. *et al.* MOLEonline: a web-based tool for analyzing channels, tunnels and pores (2018 update). *Nucleic Acids Res.* **46**, W368–W373 (2018).

73. Jurrus, E. *et al.* Improvements to the APBS biomolecular solvation software suite. *Protein Sci. Publ. Protein Soc.* **27**, 112–128 (2018).

74. Perez-Riverol, Y. *et al.* The PRIDE database resources in 2022: a hub for mass spectrometry-based proteomics evidences. *Nucleic Acids Res.* **50**, D543–D552 (2022).

75. Matias, V. R. F., Al-Amoudi, A., Dubochet, J. & Beveridge, T. J. Cryo-Transmission Electron Microscopy of Frozen-Hydrated Sections of Escherichia coli and Pseudomonas aeruginosa. *J. Bacteriol.* **185**, 6112–6118 (2003).

76. Li, L. *et al.* Structure of the ISW1a complex bound to the dinucleosome. *Nat. Struct. Mol. Biol.* **31**, 266–274 (2024).

Acknowledgements

The Novo Nordisk Foundation Center for Protein Research is supported financially by the Novo Nordisk Foundation (NNF14CC0001). N.M.I.T. acknowledges support from an NNF Hallas-Møller Emerging Investigator grant (NNF17OC0031006), an NNF Hallas-Møller Ascending Investigator grant (NNF23OC0081528) and an NNF Project grant (NNF21OC0071948). N.M.I.T. is also a member of the Integrative Structural Biology Cluster (ISBUC) at the University of Copenhagen. H.H. acknowledges support from Lundbeck Foundation postdoc fellowship R347-2020-2429. S.A.J. acknowledges support from the Health Research Council of New Zealand (Sir Charles Hercus Fellowship) and from Bioprotection Aotearoa (Tertiary Education Commission, New Zealand). We also acknowledge the use of the New Zealand eScience Infrastructure (NeSI) high-performance computing facilities in this research. T.C.D.H. was supported by a University of Otago Doctoral Scholarship. P.F.P. and M.E. acknowledge funding by the Deutsche Forschungsgemeinschaft (DFG, German Research Foundation) – Projektnummer 548567920 in the framework of the priority program SPP2330, M.E. acknowledges funding by the European Research Council (ERC) under the European Union's Horizon 2020 research and innovation programme (grant agreement n˚864971) and by the Max Planck Society as Max Planck Fellow. V.K.S and N.N.R. acknowledge support from Novo Nordisk Bioscience Ph.D. program, NNF0069780 and NNF0078229, respectively. Y.W. acknowledges support from the National Key Research and Development Program of China (2021YFF1200404), the National Science Foundation of China (32371300), and computational resources from the Information Technology Center and State Key Lab of Computer-Aided Design (CAD) & Computer Graphics (CG) of Zhejiang University. M.L.N. lab was supported by the Novo Nordisk Foundation (NNF14CC0001), The Danish Council of Independent Research (grant agreement numbers 4002-00051, 4183-00322A and 8020-00220B), and The Danish Cancer Society (grant agreement R146-A9159-16-S2). A.H. and D.H. acknowledge funding by a Starting Grant (TMSGI3_211369) of the Swiss National Science Foundation (SNSF). We thank the Danish Cryo-EM Facility at the Core Facility for Integrated Microscopy (CFIM) at the University of Copenhagen and Tillmann Pape and Nicholas Heelund Sofos for support during data collection. We thank Blanca Lopez Mendez and Morten Ib Rasmussen for their support in Mass Spectrometry and Mass Photometry.

Author contribution

N.M.I.T. and H.H. conceived the project. H.H., A.R-E., and N.R.R. and F.J.O.M. did molecular biology and mutagenesis. H.H. expressed, purified, optimized, prepared cryo-EM grids, collected cryo-EM data, and determined all the structures presented in this study. P.F.P. carried out and analyzed time-lapse, TIRF and labeled phage microscopy experiments. P.F.P together with M.E. interpreted the microscopy studies. M.E. labeled phages and performed the Western blot of the

ZorB-HaloTag fusions. S.A.J. and T.C.D.H. performed phage infectivity, adsorption, and phage burst assays. S.A.J. performed cell survival, conjugation, and transformation assays. S.A.J. and L.J.P. performed bioinformatic analyses. N.R.R. and F.J.O.M. assisted with protein purification. N.R.R., F.J.O.M. and H.H. optimized the nuclease and EMSA experiments. N.R.R obtained the ZorC-DNA complex dataset. A.R-E. and V.K.S. purified phage genomes. D.H. and A.H generated the Bas54-*parS* phage. Y.W. and Y.Y. helped with ZorA tail structure modeling. H.H. prepared samples for mass spectrometry. I.A.H. and M.L.N. performed mass spectrometry and analyzed the data. N.R.R., H.H. and I.S. performed PG binding assays. H.H. and S.A.J. prepared figures and H.H. wrote the first draft of the manuscript together with N.M.I.T. and S.A.J. with input from all the authors. This draft was then edited by M.E., P.F.P. and R.B., and all the other authors. H.H., S.A.J., M.E., P.F.P. and N.M.I.T. provided the supervision of the manuscript.

Competing Interests

The authors declare no competing interests.

Data and Code Availability

Atomic coordinates for ZorAB WT, ZorA$^{E86A/E89A}$ZorB, ZorA$^{\Delta 359-592}$ZorB and ZorA$^{\Delta 435-729}$ZorB were deposited in the Protein Data Bank (PDB) under accession codes 8QYD, 8QYH, 8QYK, 8QYY, respectively. The corresponding electrostatic potential maps were deposited in the Electron Microscopy Data Bank (EMDB) under accession codes EMD-18751, EMD-18754, EMD-18756, EMD-18766, respectively. The local refinement map of ZorB PGBD in ZorAB WT were deposited in the EMDB under accession code EMD-18752. Atomic coordinates for ZorC were deposited in the PDB under accession code PDB: 8R68. The corresponding electrostatic potential maps was deposited in the EMDB under accession code EMDB: EMD-18848. Atomic coordinates for ZorD apo form and its complex with ATP-γ-S were deposited in the PDB under accession codes PDB: 8QY7 and 8QYC, respectively. The corresponding electrostatic potential maps were deposited in the EMDB under accession codes EMD-18747 and EMD-18750. The mass spectrometry proteomics data have been deposited to the ProteomeXchange Consortium via the PRIDE[74] partner repository with the dataset identifier PXD047450.

Extended Data Legends:

Extended Data Figure 1. *E. coli* Zorya type I protects against phage invasion but not bacterial conjugation or plasmid transformation.

a, Zorya system gene arrangements for each Zorya type (I–III), with typical gene annotations shown. **b,** Phylogeny of the ZorA motor sequence (excluding the ZorA tail) rooted with the *E. coli* MotA (*Ec*MotA) sequence. **c,** Taxonomic analyses of Zorya hosts, using the GTDB phyla-level taxa. Each phylum was assigned as either possessing a single membrane cell envelope (Monoderm) or double membrane envelope (Diderm). In some cases, there are both monoderm and diderm species within phyla, which are labeled as 'Both'. The number of genomes analyzed for each phyla (*n* genomes) is based on the genomes present in the GTDB v214.1 and RefSeq v209. **d**, The impact of *Ec*ZorI on the uptake of plasmid DNA via conjugation from an *E. coli* donor strain, measured as the transconjugant frequency (number of transconjugants/total recipients). Four plasmids with different origins of replication (OriV) were tested (ColE1, RSF1010, pBBR1 and RK2), at the indicated donor to recipient cell ratios (D:R) for the matings. Data represent the mean of three replicates. **e**, The impact of *Ec*ZorI on the uptake of plasmid DNA via transformation. Chemically competent *E. coli* without (control; empty vector) or with *Ec*ZorI were transformed with plasmids possessing either ColE1 or pBBR1 origins of replication. Data represent the mean of three replicates, with each replicate being a different batch of competent cells. **f,** Infection time courses for liquid cultures of *E. coli*, with and without *Ec*ZorI, infected at different multiplicities of infection (MOI) of phage Bas24 (early timepoints for MOI 1 and 10, from Fig 1e). **g**, Infection time courses for liquid cultures of *E. coli*, with and without *Ec*ZorI, infected at different multiplicities of infection (MOI) of phage Bas02 and Bas08. **h**, Phage titers at the end timepoint for each sample from the infection time courses (**g**), measured as EOP on indicator lawns of *E. coli* either without (control) or with *Ec*ZorI. LOD: Limit of detection. Data in **f-h** represent the means of 3 replicates and the shaded regions represent the SEM.

Extended Data Figure 2. Cryo-EM dataset processing results and resolution of *Ec*ZorAB.
a, A representative SDS gel of the purified *Ec*ZorAB complex. **b**, An EM image of the *Ec*ZorAB sample under the cryogenic condition. **c**, Cryo-EM density map of *Ec*ZorAB colored by local resolution (in Å) estimated in cryoSPARC. **d**, Gold standard (0.143) Fourier Shell Correlation (GSFSC) curves of refined *Ec*ZorAB complex. **e**, Cryo-EM map of *Ec*ZorAB. **f**, Representative model segment of ZorA fit into EM density, focusing on TM1 of one of the ZorA subunits. **g**, Volcano plot analysis, visualizing ratio and significance of change between all proteins quantified by mass spectrometry in *E. coli* total lysates either transformed with p*Ec*ZorI plasmids or not (**Supplementary Table 1**). Significance was tested via two-tailed two-sample Student's t-testing with permutation-based FDR control, ensuring a corrected p-value of < 0.01. n=4 technical replicates derived from n=3 culture replicates. **h**, Absolute copy number analysis of Zorya proteins expressed in *E. coli*. Determined via comparison of molecular weight-adjusted label-free quantified protein abundance values from this study, to known copy numbers reported by Schmidt et al.[56], and establishing a "proteomic ruler" for conversion of measured abundance values to approximate copy numbers (**Supplementary Table 1**). n=4 technical replicates derived from n=3 culture replicates. **i**, Soft mask used for local refinement of the ZorB PGBDs. **j**, Local refinement map of the ZorB PGBDs (made with the soft mask shown in **i**), colored by local resolution. **k**, A

representative of a model segment of the ZorB PGBDs fitted into of the local refinement EM density map shown in **j**, focusing on the PGBD dimerized interface. **l**, Fit of lipids found in the TMD of ZorA in the *Ec*ZorAB cryo-EM map. Images in **a** and **b** are representatives of at least 3 replicates.

Extended Data Figure 3. *Ec*ZorA tail secondary structural prediction and a complete composite model of *Ec*ZorAB complex.

a, Amino acids and secondary structural predictions (Psipred) of the *Ec*ZorA. The peptides found by mass spectrometry that covered ZorA protein are indicated as green lines above the amino acids. **b,** Top hits from an HHpred sequence homology search of the ZorA tail are shown. **c**, A composite model of *Ec*ZorAB with the ZorA tail folding into a pentameric super coiled-coil, with the helical pitch of the tail α-helix shown. **d**, Hydrophobicity of the tail tube exterior surface calculated by ChimeraX. **e**, Hydrophobicity and polarity of the tail tube interior surface calculated by MOLE*online*.

Extended Data Figure 4. Structure of *Ec*ZorAB and its function as a peptidoglycan binding rotary motor.

a, Cartoon representation of the *Ec*ZorAB complex in an inactive state, with the ZorB dimer interfaced highlighted. **b**, Topology diagrams of ZorB PGBDs and isolated crystal structures of the flagellar stator unit MotB and PomB PGBDs, indicating a conserved folding architecture. **c**, The two disulfide bonds identified from ZorB PGBDs, with the EM map overlapped. **d**, Structural comparison of PGBD of *Ec*ZorB with that of ProE that in complex with PG fragment, with the zoom in view highlighting the conserved residues from *Ec*ZorB that are likely involved in PG binding. **e**, Structural comparison of *Ec*ZorB PGBD and AlphaFold3 predicted *Ec*MotB PGBD, highlighting *Ec*ZorB PGBD is fused without a linker to the ZorB TM. **f**, *In vitro* pull-down assay of isolated *Ec*ZorAB complex with purified *E. coli* PG. **g**, *In vitro* pull-down assay of isolated *Ec*ZorAB complex and *Ec*ZorAB complex with mutations in the ZorB PGBD ($ZorAB^{Y151A/N152A/L155A/R159A}$) with purified *E. coli* PG. **h**, *In vitro* pull-down assay of isolated ZorB PGBD, mutant ZorB PGBD ($ZorB^{Y151A/N152A/L155A/R159A}$ PGBD), MotB PGBD (positive control) and ZorE (negative control) with purified *E. coli* PG. **i**, Cross-section view of the *Ec*ZorAB TMD, showing the surrounding residues of the two Asp26 from ZorB. **j**, Cartoon representation of the cryo-EM structure of the proton-driven flagellar stator unit MotAB from *Campylobacter jejuni* (*Cj*MotAB) in its inactive state, with the MotB plug motif highlighted. **k**, Cross-section view of the *Cj*MotAB TMD, showing the surrounding residues of the two Asp22 from MotB. **l**, Cartoon representation of the cryo-EM structure of the sodium-driven flagellar stator unit PomAB from *Vibrio alginolyticus* (*Va*PomAB) in its inactive state. **m**, Cross-section view of *Va*PomAB TMD, showing the surrounding residues of the two Asp24 from PomB. The absence of the strictly conserved threonine residue on ZorA TM3 (**k**) required for sodium ion binding, indicates that *Ec*ZorAB is a proton-driven stator unit. **n**, A representative of an SDS gel of the purified *Ec*ZorAB 'linker mutant' complex (with ZorB residues 46-52 replaced by a GGGSGGS linker). **o**, A

representative cryo-EM image of *Ec*ZorAB 'linker mutant' sample. **p**, Representative 2D classes of the *Ec*ZorAB 'linker mutant' in comparison with that of the *Ec*ZorAB wild type, highlighting the flexibility of the ZorB PGBDs in the mutant. **q**, A representative negative stain EM image of *Ec*ZorAB 'PG-binding mutant' sample. **r**, Low pass filter of the cryo-EM density map of the *Ec*ZorAB linker mutant after non-uniform refinement. **s**, Transmembrane helix density of the *Ec*ZorAB 'linker mutant' and that in the wild type *Ec*ZorAB. Images in **f**, **g**, **h**, **n**, **o**, **q** are representatives of at least 3 replicates with similar results.

Extended Data Figure 5. *Ec*ZorAB Ca^{2+} binding site and tail influence ZorAB motor assembly and function.

a, ZorA tail truncations indicated in the composite model of *Ec*ZorAB complex. **b**, Cartoon representation of the *Ec*ZorAB ZorA single subunit. **c**, Interaction between the beginning of the ZorA tail and the β-hairpin motif. **d**, Extra density found inside the tail from cryo-EM map, which was modeled as a palmitic acid molecule, with the amino acids involved in the interactions indicated. **e**, Structural comparison of the ZorA wild type (cyan) and ZorA Ca^{2+} binding site mutation ($ZorA^{E86A/E89A}$, gray), the arrows highlight the changes from wild type to the mutant. **f**, Predicted ZorA lipid binding sites using PeSTo. **g**, An EM image of the *Ec*$ZorA^{L250G/L254G/L258G/L261G}$ZorB mutant under the cryogenic condition and representative 2D classes. **h**, An EM image of the *Ec*$ZorA^{L250N/L254N/L258N/L261N}$ZorB mutant under the cryogenic condition and representative 2D classes. **i**, An EM image of the $ZorA^{\Delta 223-729}$ZorB mutant under the cryogenic condition and representative 2D classes. **j**, Negative staining images of the *Ec*ZorAB wild type, ZorA tail middle deletion ($ZorA^{\Delta 359-592}$), ZorA tail tip deletion ($ZorA^{\Delta 435-729}$). **k**, The tail lengths of the *Ec*ZorAB wild type, ZorA tail middle deletion ($ZorA^{\Delta 359-592}$), ZorA tail tip deletion ($ZorA^{\Delta 359-592}$) as measured in (**g**). Data represent the mean of at least eight measurements (data points indicate measurements), and error bars represent the standard error of the mean (SEM). **l-m**, Cryo-EM maps and resolutions of ZorA mutants with gold standard (0.143) Fourier Shell Correlation (GSFSC) curves.

Extended Data Figure 6. The effects of *Ec*Zorya mutations on *Ec*ZorI-mediated anti-phage defense and long ZorA tails are conserved amongst Zorya system types in diverse species.

a, Effects of ZorA, ZorB, ZorC and ZorD mutations on *Ec*ZorI-mediated anti-phage defense, as measured using EOP assays with phages Bas02, Bas19 and Bas25. Data represent the mean of at least 3 replicates (data points indicate replicates) and are normalized to the control samples lacking *Ec*ZorI. **b**, The ZorA tail lengths found in different Zorya system types. Motor and tail lengths were determined by inspecting the predicted structures of several representative ZorA sequences, then inferring these lengths for the rest of the ZorA sequences through sequence alignment (methods). The reduce sequencing bias, unique Zorya systems encoded in RefSeq (v209) bacteria and archaea genomes were selected based on their distinct genomic context (methods). **c**, Time-lapse, phase contrast microscopy of *E. coli* cells expressing empty vector control, *Ec*ZorI wt, *Ec*ZorI $ZorB^{D26N}$ and *Ec*ZorI $ZorA^{483-729}$ exposed to Bas24 at an MOI of 5. **d**, Quantitation of the

time-lapse microscopy in (c), displaying the measured cell area relative to the first timepoint of the time-lapse. Data represent the means of three biological replicates and the shaded region indicate standard deviation. **e**, Quantitative Western blot of selected *Ec*ZorI-HaloTag translational fusions. Top: total protein stain of whole cell lysate. Bottom: Anti-HaloTag (mouse, Promega) Western blot against ZorB-HaloTag protein fusions. Mean ± standard deviation from four biological replicates.

Extended Data Figure 7. Structural and functional investigation of *Ec*ZorC and *in vivo* DNA degradation.

a, SDS gel of purified ZorC wild type, ZorC^{E400A}, ZorC^{H443A}, ZorC$^{\Delta CTD}$ (deletion residues 487-560). Gel is representative of at least 3 replicates. **b**, Unsharpened Cryo-EM map of *Ec*ZorC. **c**, Local refinement of the *Ec*ZorC core domain with a soft mask, with the local resolution (in Å) estimated in cryoSPARC. **d**, Gold standard (0.143) Fourier Shell Correlation (GSFSC) curves of the local refined of the *Ec*ZorC core domain. **e**, Representative of a model and segments of the ZorC fitted into EM density map. The right panel is the final model of *Ec*ZorC built from a cryo-EM map. **f**, AlphaFold3-predicted ZorC model. **g**, Electrostatic distribution of *Ec*ZorC calculated from AlphaFold3-predicted model. **h**, *In vitro* interaction of *Ec*ZorC with 55 bp dsDNA (36.36% GC), 18bp dsDNA (50.00% GC), 18bp dsDNA (22.22% GC), 18bp dsDNA (72.22% GC). Image is representative of at least 3 replicates. DNA sequences are shown below. **i**, AlphaFold3-predicted model of ZorC in complex with 18 bp dsDNA. The color code (per-atom confidence estimate on a 0-100 scale) in **f** and **i** are same. **j**, Representative time-lapse images of *E. coli* cells expressing ParB-mSc in the presence or absence of EcZorI, exposed to Bas54-*parS* phage. In *Ec*ZorI-null cells, ParB foci are observed prior to cell lysis, whereas *Ec*ZorI-expressing cells lack ParB focus formation and survive phage infection. Scale bar is set to 2 μm.

Extended Data Figure 8. *Ec*ZorD is autoinhibited nuclease.

a, Representative of the SDS gel of the purified ZorD wild type, ZorD$_{CTD}$ (residues 503-1080), ZorD$_{NTD}$ (residues 1-502), ZorD$_{CTD}^{D730A/E731A}$ and ZorD$_{CTD}^{E651A}$. Gel is representative of at least 3 replicates. **b**, Cryo-EM map of the *Ec*ZorD apo form. **c**, Cryo-EM map and structure of *Ec*ZorD in complex with ATP-γ-S. A zoomed-in view of the ATP-γ-S binding site is depicted, with the cryo-EM map overlayed on the ATP-γ-S molecule. **d**, Structural comparison of the *Ec*ZorD apo from (gray) and *Ec*ZorD in complex with ATP-γ-S (light purple); the arrows highlight the changes from apo form to the ligand-bound form. **e**, ZorD$_{CTD}$ degrades phage Bas08 and Bas58 genomic DNA (gDNA). Gel is representative of 3 replicates. **f,** *Ec*ZorD WT and its isolated C-terminal domain nuclease activity in the absence and presence of *Ec*ZorC. **g,** *Ec*ZorC dsDNA binding activity in the absence and presence of *Ec*ZorD. **h,** AlphaFold3 predicted model of *Ec*ZorD in complex with 18 bp dsDNA and ATP, showing an alternative, open conformation of ZorD. **i,** ZorD-DNA interaction in the AlphaFold3 predicted model; key residues are highlighted. **j,** Structural superimposition of the cryo-EM structure of *Ec*ZorD with the AlphaFold3 predicted *Ec*ZorD in complex with dsDNA model**.** The arrow indicates the possible conformational

transition of the *Ec*ZorD NTD. **k,** Zoom in from **j** highlighting that the NTD of *Ec*ZorD in the DNA free state clashes with DNA in the ZorD–DNA complex model. **l,** Superimposition of the AlphaFold3 predicted model ZorD–DNA complex with the top hit (PDB 7X3T[76]) from Dali (Z-score = 26.6). **m,** AlphaFold3 predicted ZorD–ZorC–dsDNA-ATP-Mg^{2+} complex, with a confidence-colored (per-atom confidence estimate on a 0-100 scale) model shown in the right panel.

Extended Data Figure 9. ZorAB recruit ZorC and ZorD during phage invasion.
a, Complementation experiment between *E. coli* and *P. aeruginosa* (*Pa*) Zorya I. Schematic representation of *Ec*ZorI, *Pa*ZorI and the constructs for *Pa*ZorCD or *Pa*ZorD complementation of *Ec*ZorI gene deletions. **b**, Anti-phage defense provided by the constructs in (**a**), as measured using EOP assays for phages Bas49, Bas52 and Bas57. Data represent the mean of at least 3 replicates (data points indicate replicates) and are normalized to the control samples lacking Zorya. **c**, Strategy of fusing mNeonGreen (mNG) or HaloTag (HT) or both into *Ec*ZorI operon. **d**, The effects of the mNeongreen (mNG) fusions to *Ec*ZorI components on anti-phage defense, as measured using EOP assays for phage Bas24. Data represent the mean of at least 3 replicates (data points indicate replicates) and are normalized to the control samples lacking *Ec*ZorI. The boxed constructs (ZorB C-terminal mNG fusion: ZorB-mNG; ZorB C-terminal HT fusion: ZorB-HT; ZorC N-terminal mNG fusion: mNG-ZorC; ZorD C-terminal mNG fusion: ZorD-mNG; Dual-tagged constructs, ZorB C-terminal HT fusion and ZorC N-terminal mNG fusion: ZorB-HT + mNG-ZorC; ZorB C-terminal HT fusion and ZorD C-terminal mNG fusion: ZorB-HT + ZorD-mNG) were used for subsequent microscopy experiments. **e**, Exemplary denoised TIRF and brightfield microscopy pictures of mNG expression driven by the *Ec*ZorI native promoter (p-mNG) either untreated or exposed to Bas24 at an MOI of 5 for 30 min. Scale bar 2 μm. **f**, Exemplary denoised TIRF microscopy pictures of ZorB C-terminal mNG fusion either untreated or exposed to Bas24 at an MOI of 5 for 30 min. Scale bar 2 μm. **g**, Comparison of detected maxima of the ZorAB complex foci between untreated or exposed to Bas24 at an MOI of 5 for 30 min (n cells > 250 from n=3 replicates), p-value: 0.030. Means are derived from three independent biological replicates. **h**, Exemplary denoised TIRF microscopy pictures of ZorD-mNG either untreated or exposed to increasing Bas24 at MOIs of 1, 5, or 50 for 30 min. **i**, Statistical comparison of ZorD-mNG maxima between untreated and conditions stated in **h**, p-values: 0.9978., 0.0009, 0.0258 and <0.0001. Means and exemplarily images in **e** and **h** derive from at least three independent biological replicates. For **g** and **i** data are presented as mean values and Tukey whiskers. Scale bar 2 μm.

Extended Data Tables

Extended Data Table 1. **Cryo-EM data collection, refinement and validation statistics.**

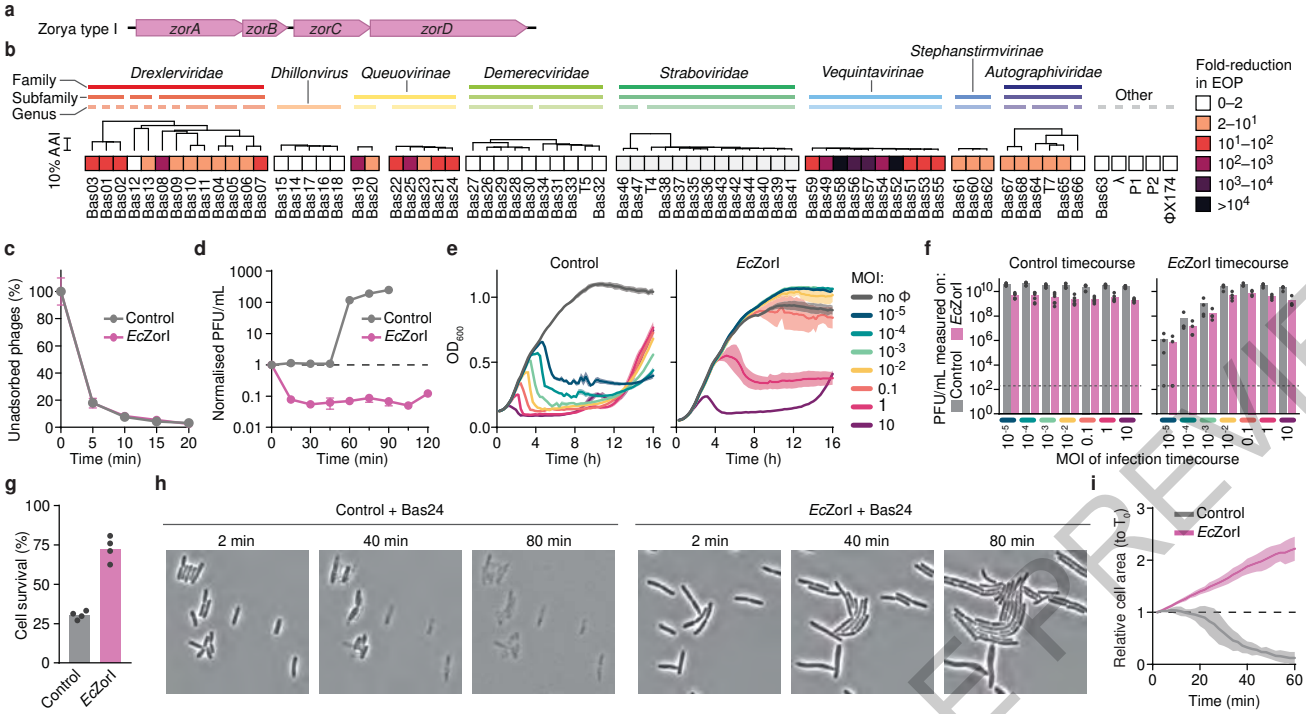

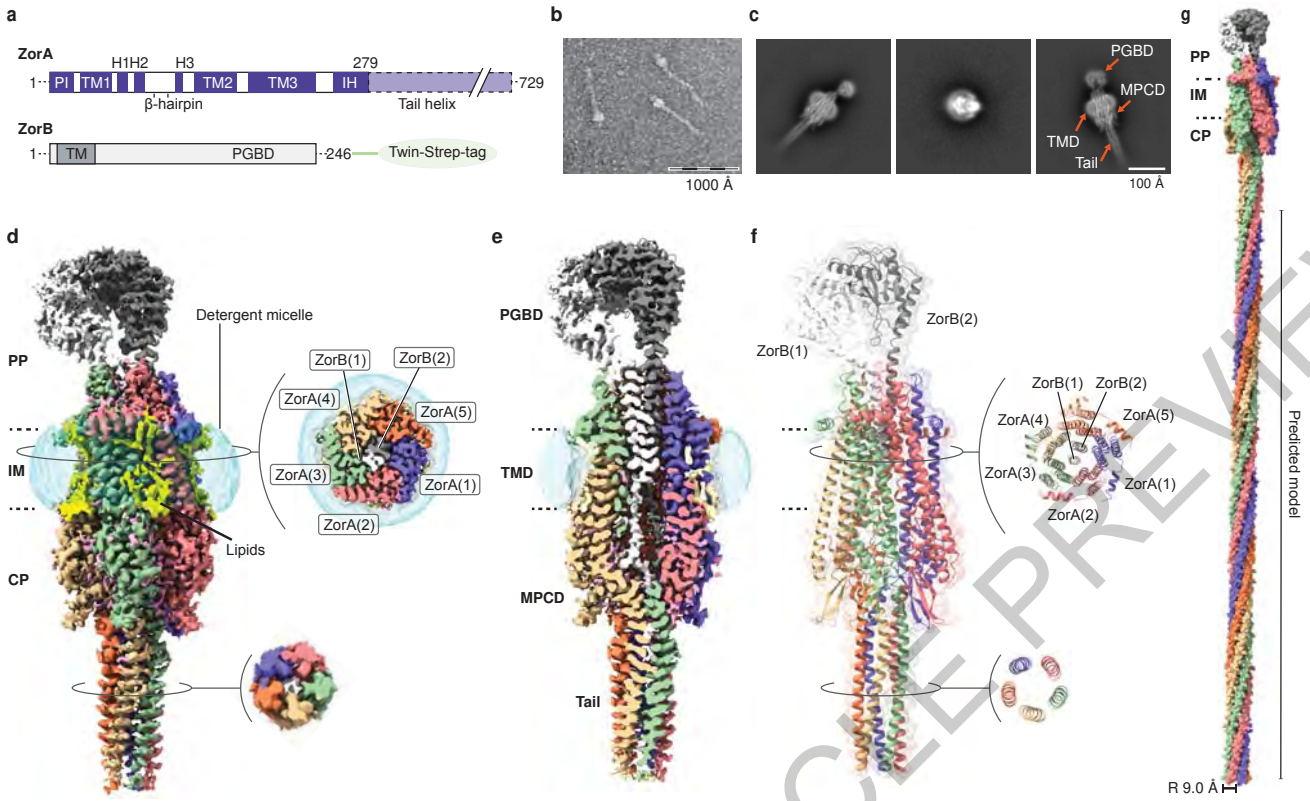

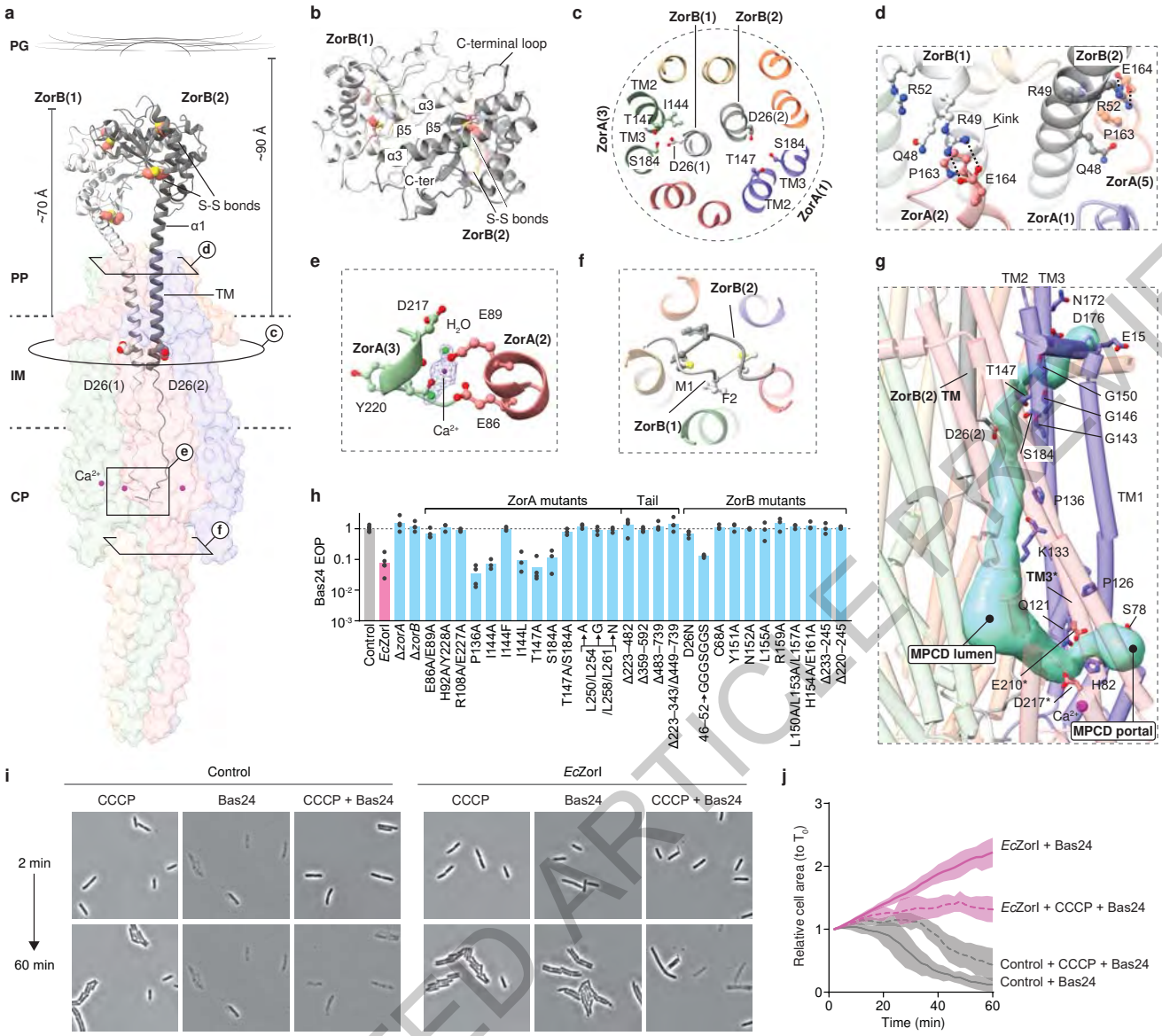

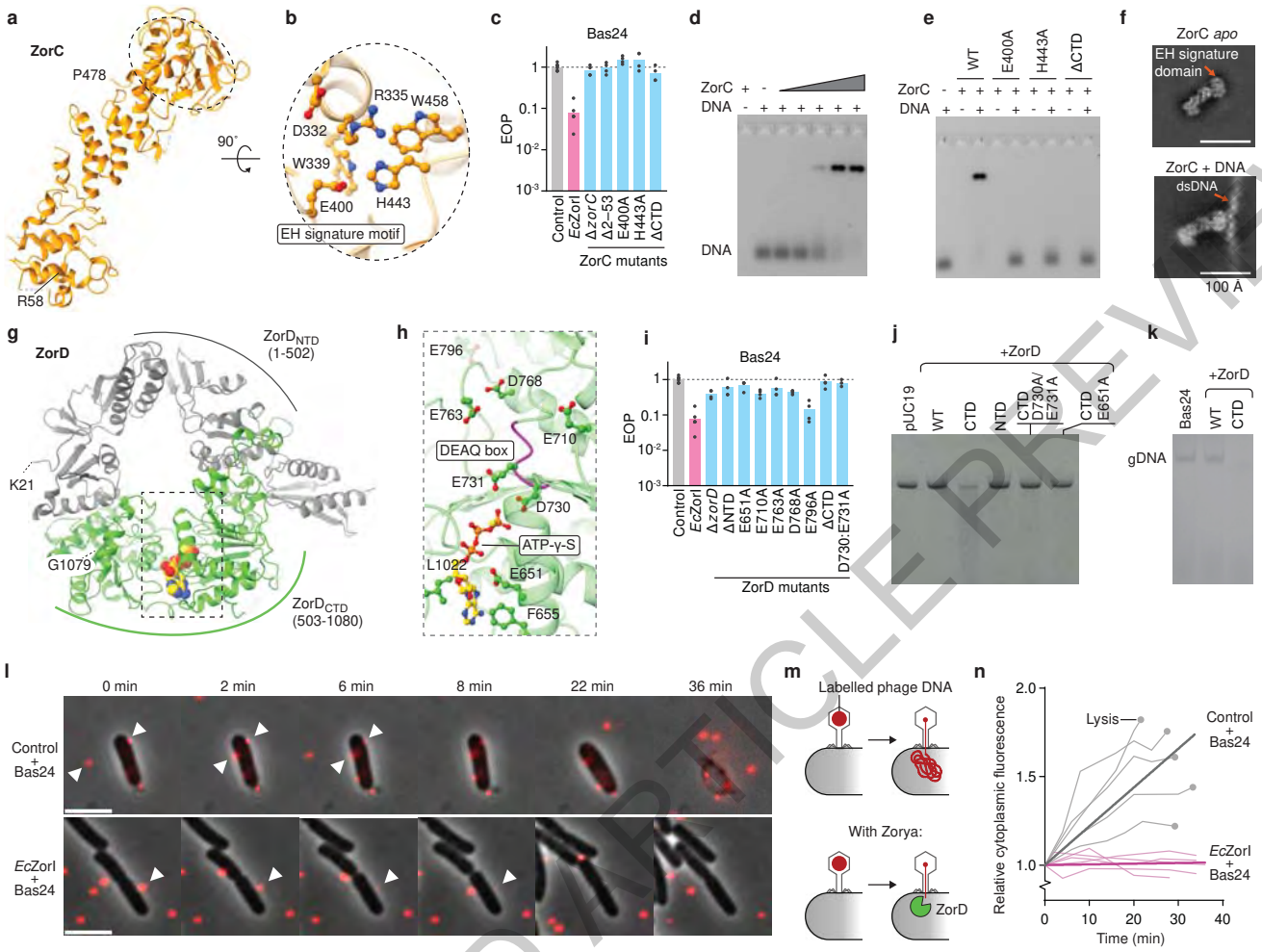

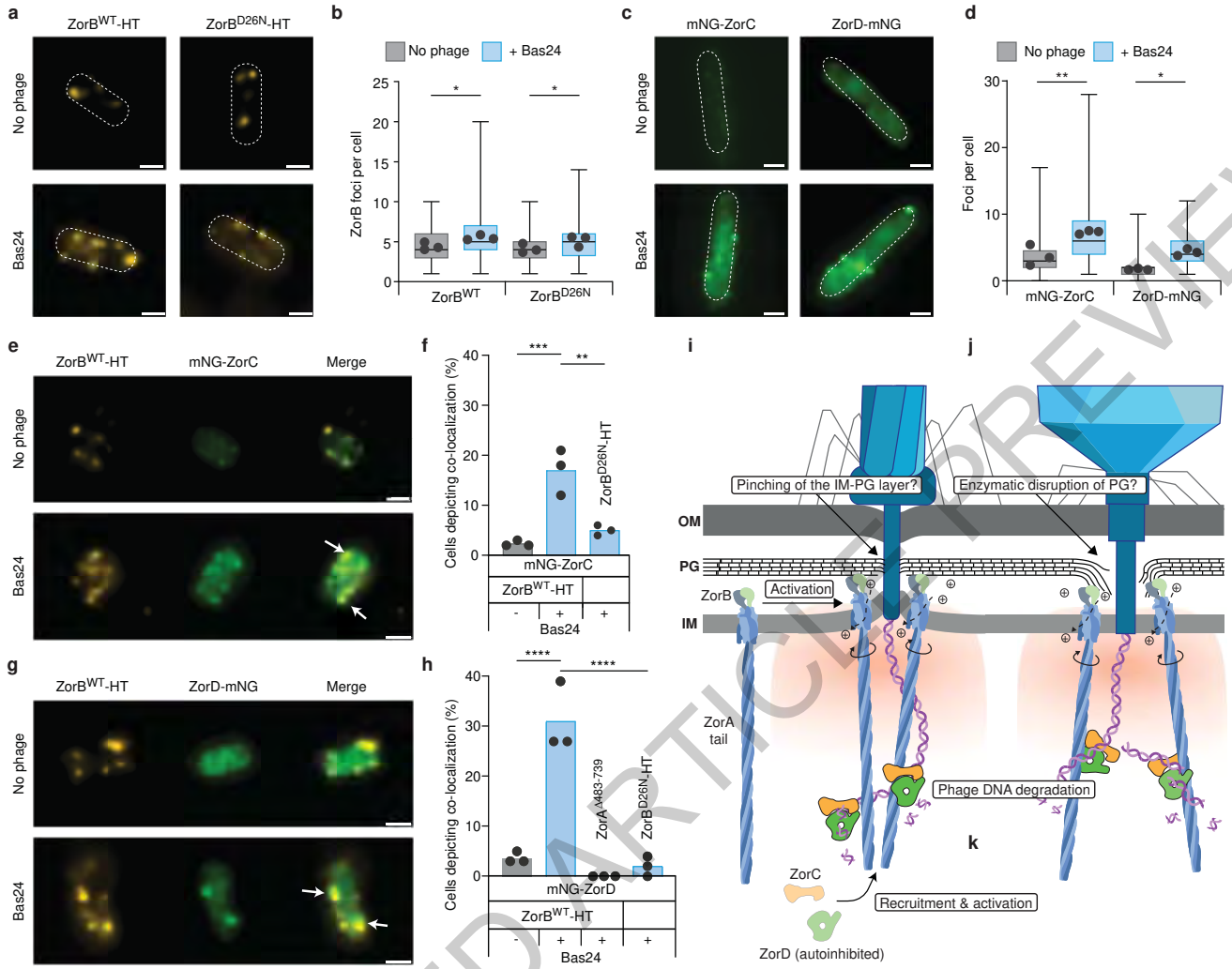

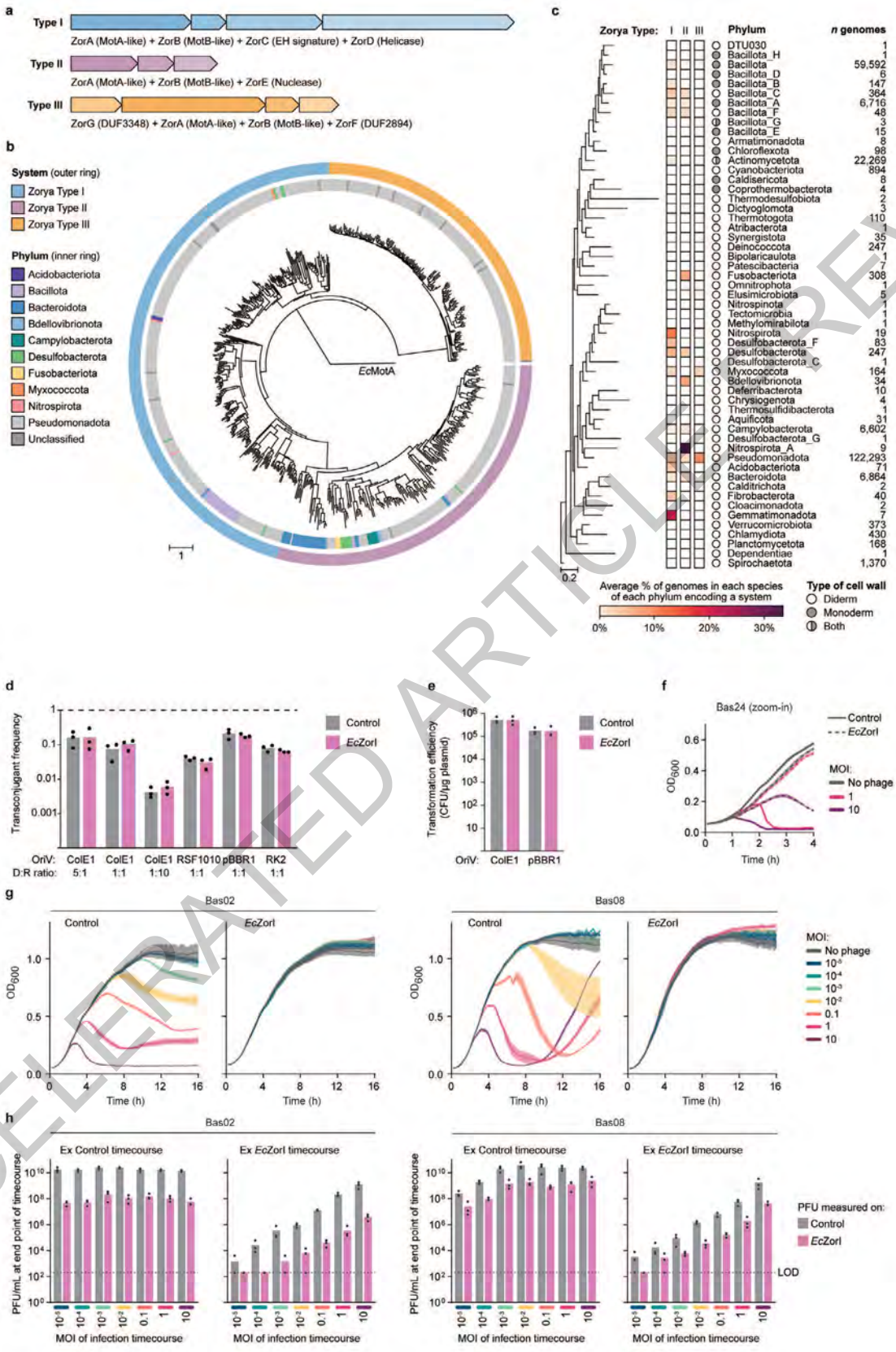

Extended Data Fig. 1

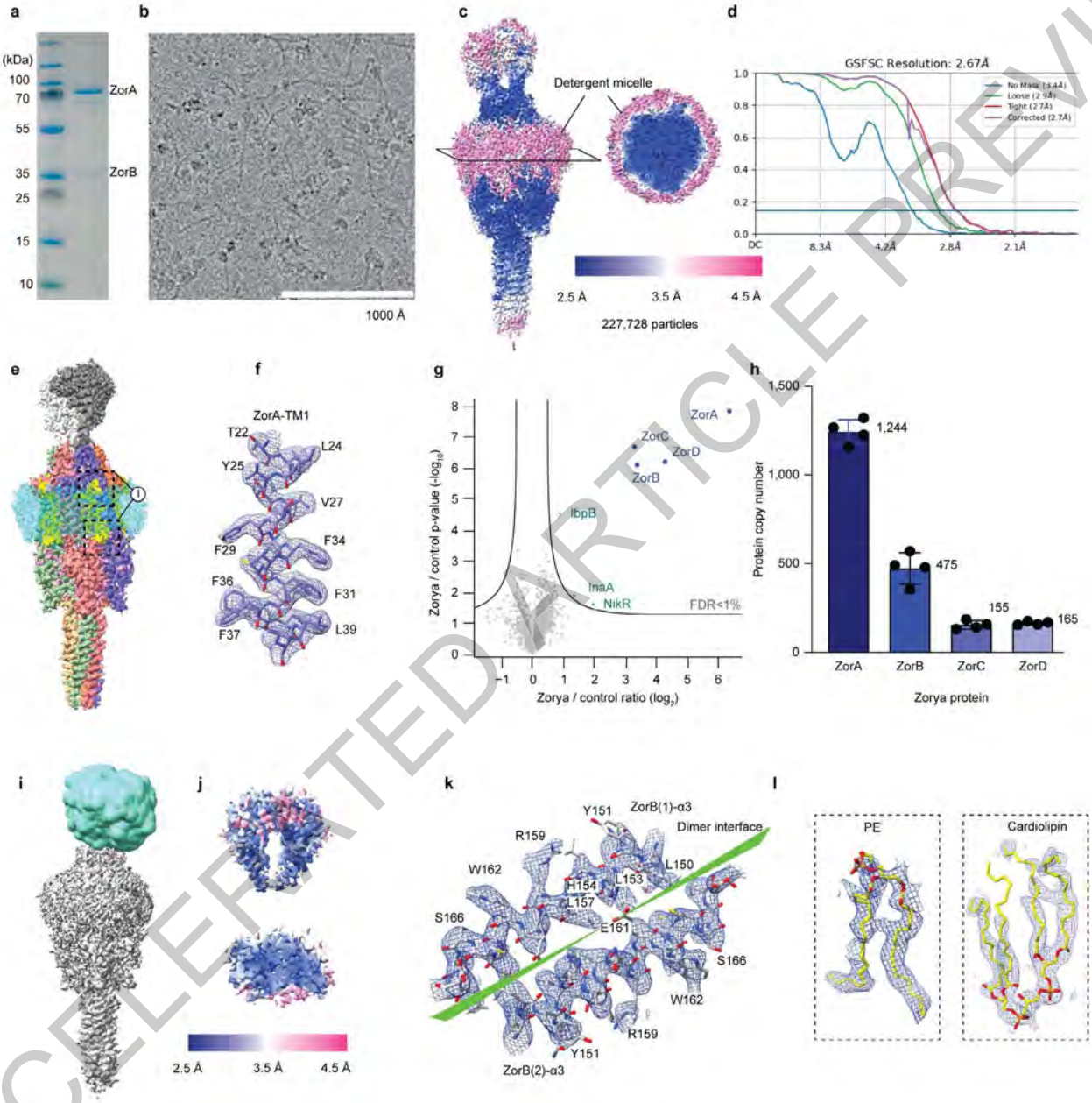

Extended Data Fig. 2

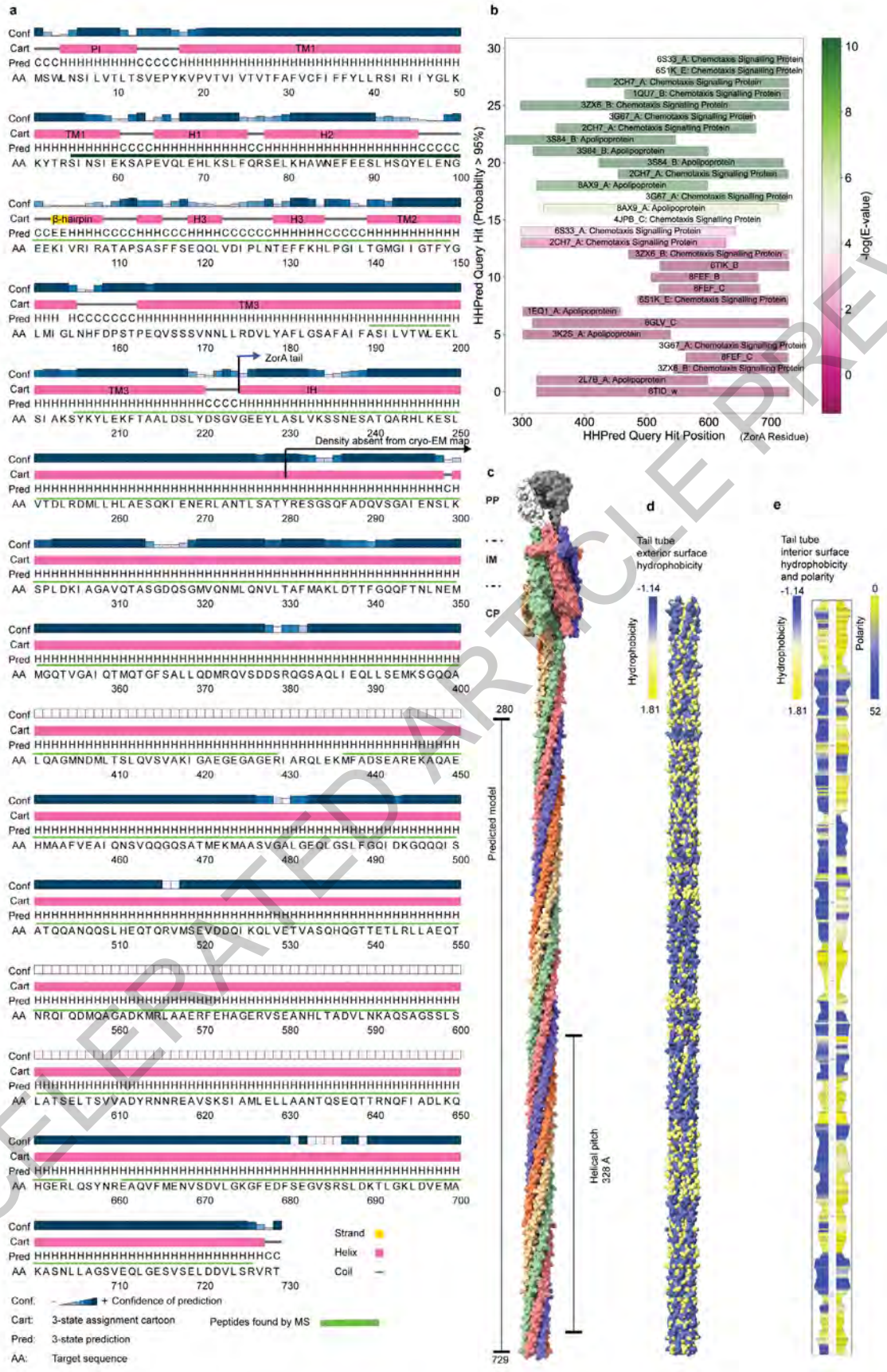

Extended Data Fig. 3

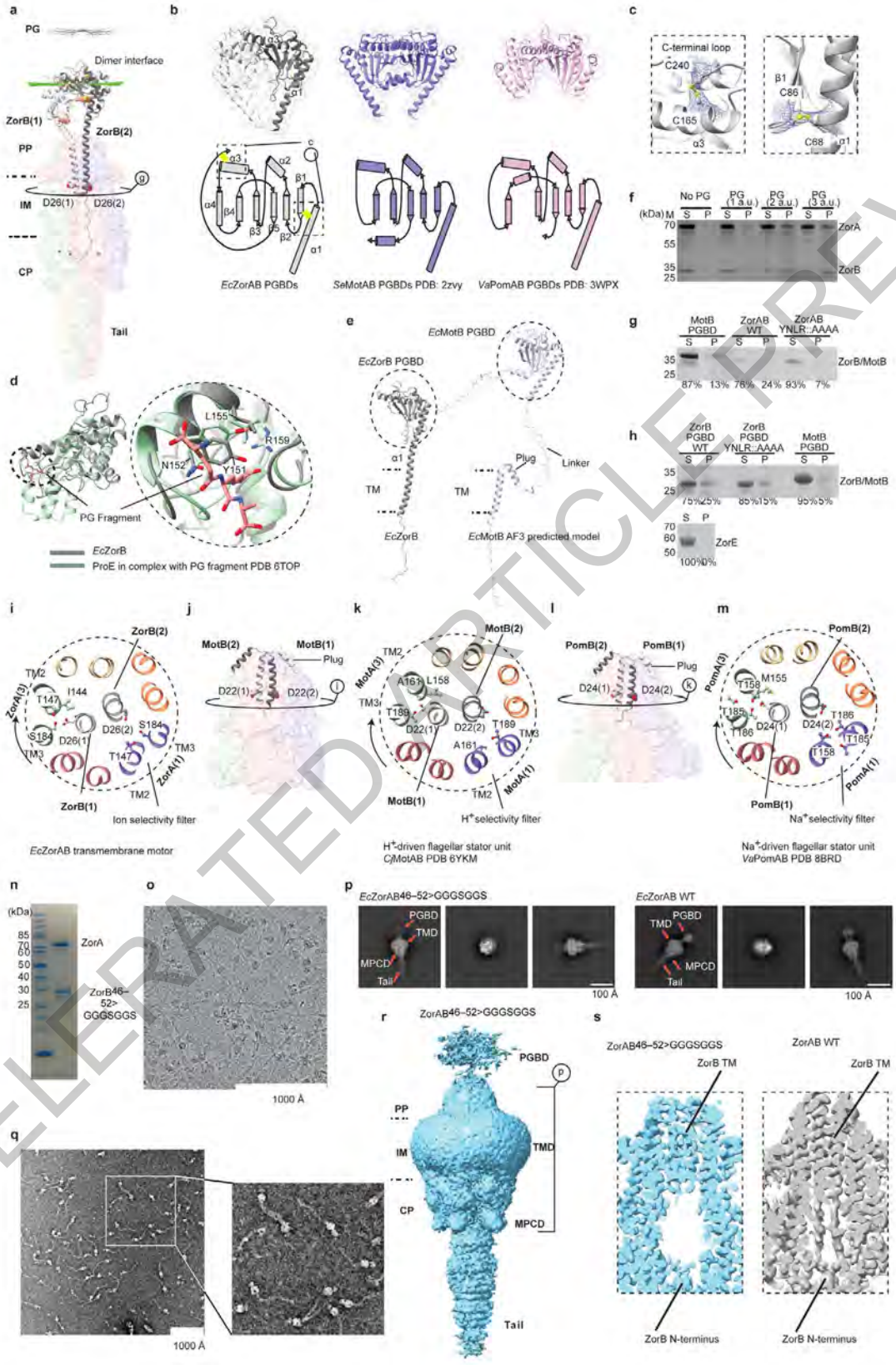

Extended Data Fig. 4

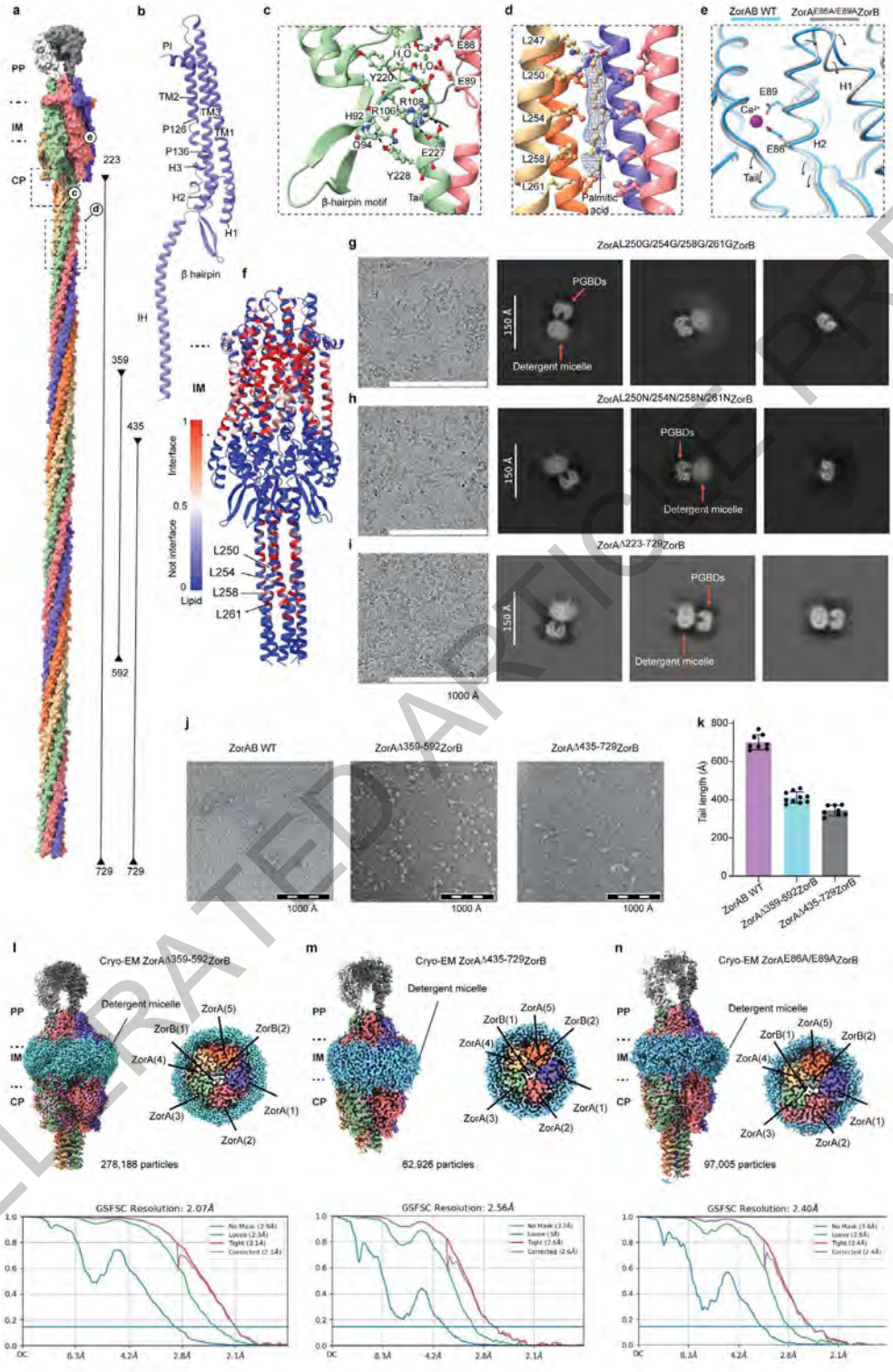

Extended Data Fig. 5

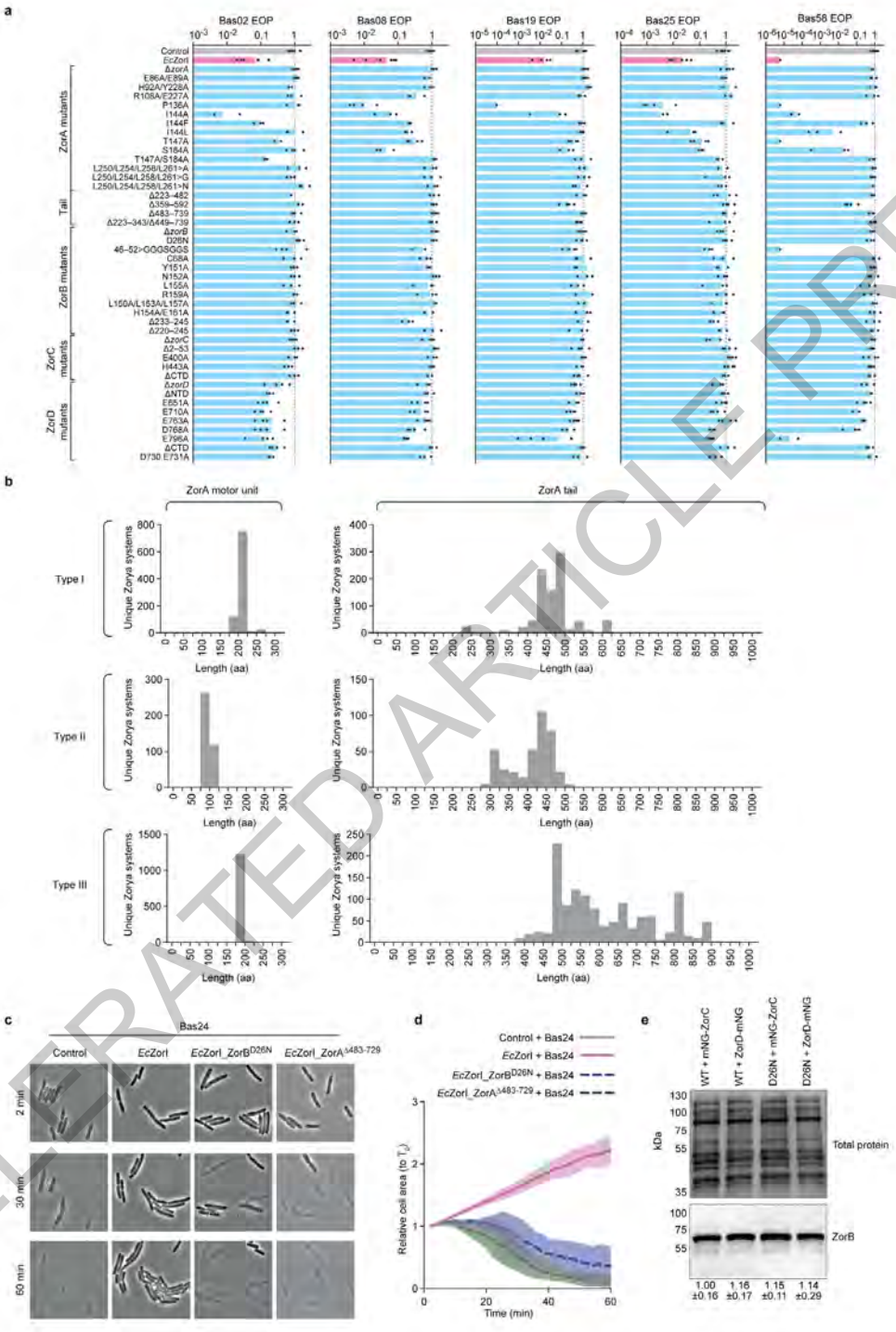

Extended Data Fig. 6

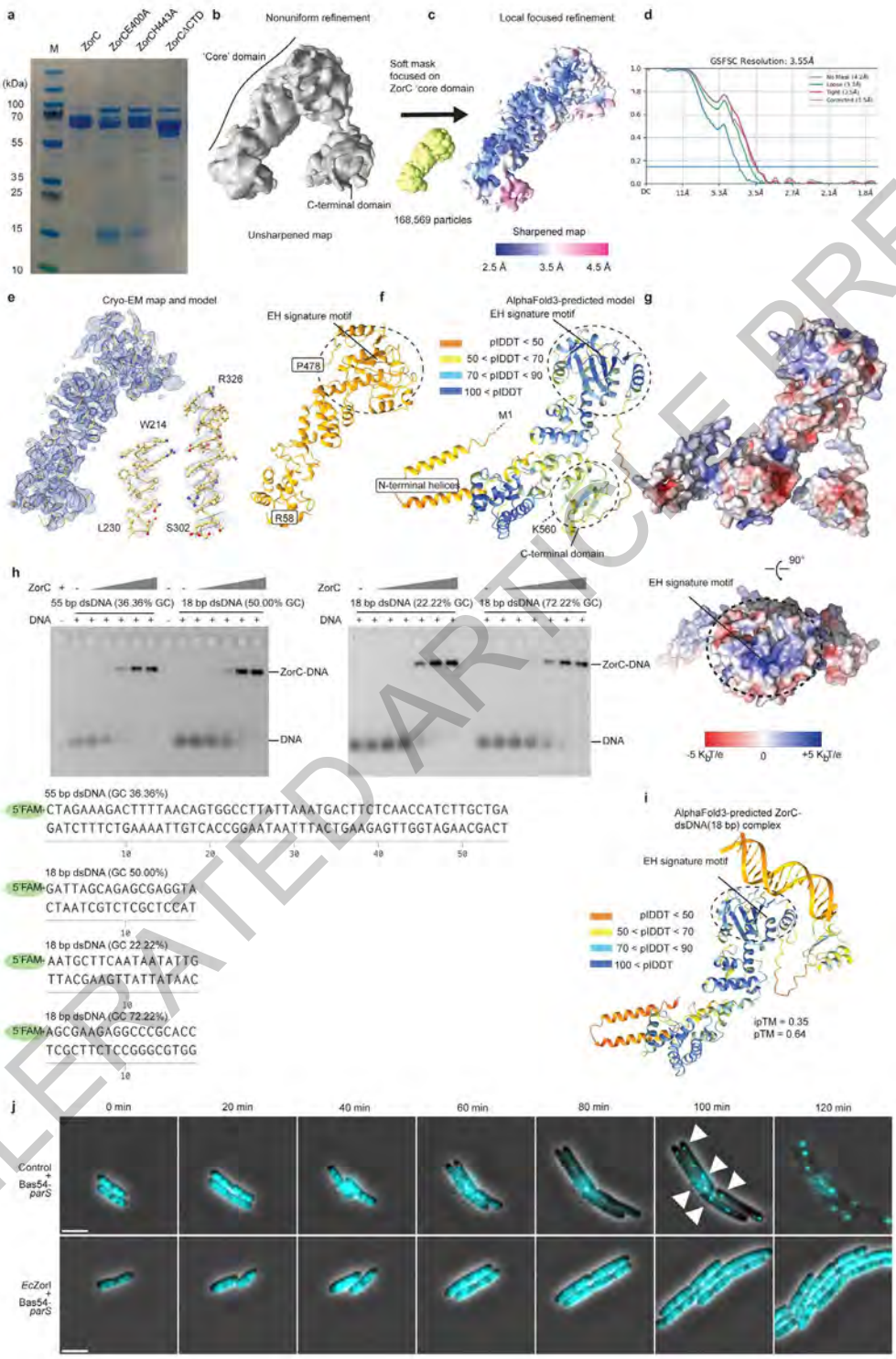

Extended Data Fig. 7

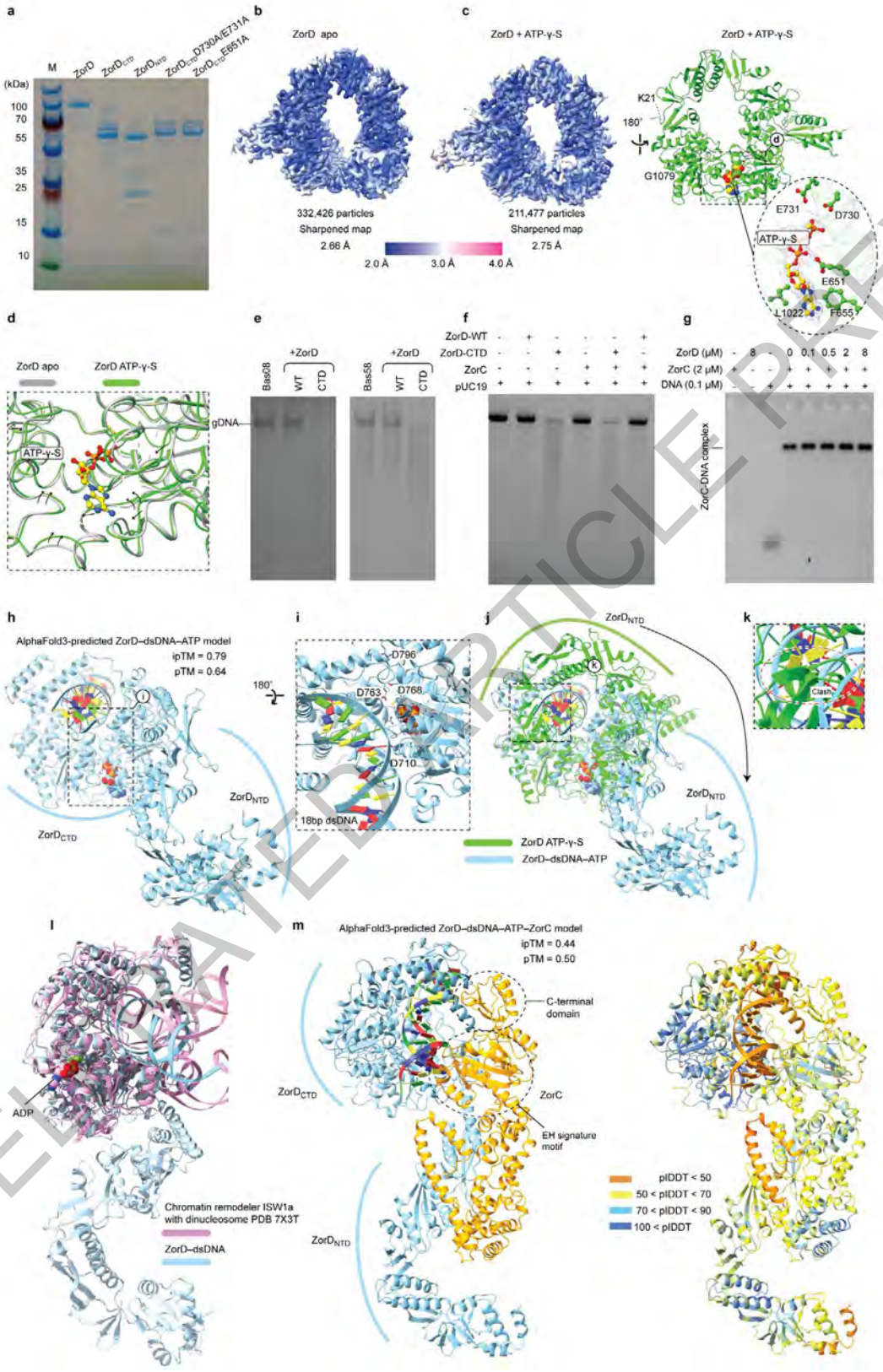

Extended Data Fig. 8

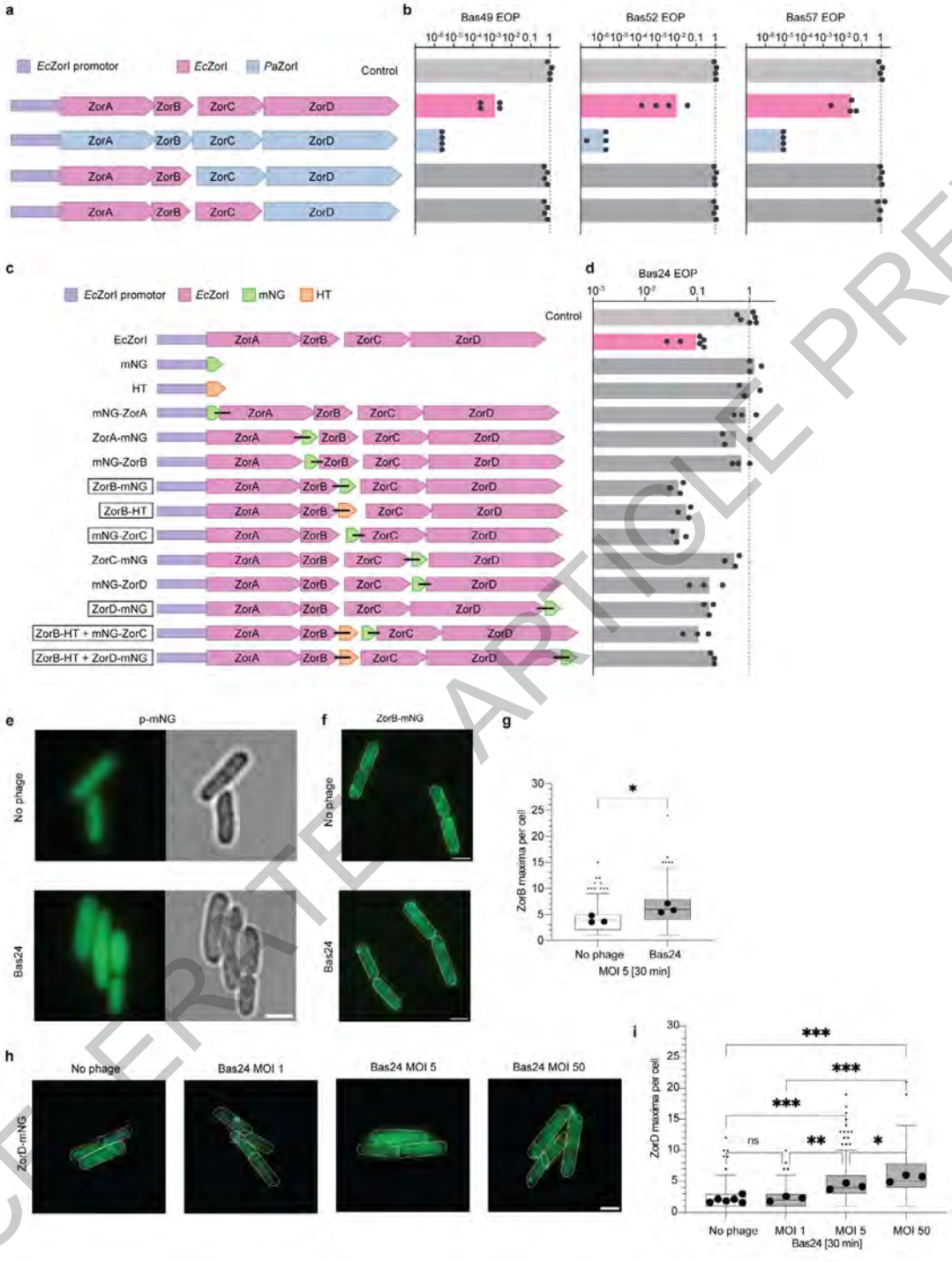

Extended Data Fig. 9

Extended Data Table 1: Cryo-EM data collection, refinement and model statistics.

	***Ec*ZorAB WT (EMDB-18751) (PDB 8QYD)**	***Ec*ZorA$^{E86A/E89A}$ZorB (EMD-18754) (PDB 8QYH)**	***Ec*ZorA$^{\Delta 359-592}$ZorB (EMD-18756) (PDB 8QYK)**	***Ec*ZorA$^{\Delta 435-729}$ZorB (EMD-18766) (PDB 8QYY)**	***Ec*ZorD apo form (EMD-18747) (PDB 8QY7)**	***Ec*ZorD + ATP-γ-S (EMD-18750) (PDB 8QYC)**	***Ec*ZorC Apo from (EMD-18948) (PDB 8R68)**
Data collection and processing							
Microscope	Titan Krios G2						
Magnification (nominal)	96,000x						
Voltage (kV)	300						
Total exposure ($e^-/Å^2$)	40.01	38.00	41.00	41.00	40.00	38.00	39.50
Exposure fractions (no.)	40						
Pixel size (Å)	0.832	0.832	0.832	0.832	0.832	0.832	0.832
Symmetry imposed	C1						
Movies used (no.)	7,700	3,203	3,181	1008	1,750	1,213	5,209
Final particles (no.)	227,728	97,005	278,186	62,926	332,426	211,477	168,569
Box size (pixels)	500	500	500	500	400	400	256
Map resolution (Å) (FSC 0.143)	2.67	2.40	2.07	2.56	2.66	2.75	3.55
Refinement							
Refinement resolution (FSC map vs. model (masked)=0.143) (Å)	2.60	2.40	2.10	2.50	2.60	2.70	3.50
Model composition							
Non-hydrogen atoms	16,154	15,925	16,182	14,829	7,168	7,199	3,240
Protein residues	1,892	1,837	1,817	1,717	893	893	391
Water molecules	313	484	866	313	n/a	n/a	n/a
B-factors (mean; $Å^2$)							
Protein	89.70	90.46	64.60	84.84	27.26	56.79	64.60
Solvent	88.61	50.89	34.01	44.93	n/a	n/a	n/a
R.m.s. deviations							
Bond lengths (Å)	0.006	0.008	0.008	0.009	0.018	0.002	0.003
Bond angles (°)	0.874	1.025	1.373	1.339	1.706	0.441	0.648
CC (mask)	0.86	0.85	0.85	0.84	0.85	0.83	0.52
Validation							
MolProbity score	1.46	1.46	1.42	1.45	1.90	1.47	2.11
Poor rotamers (%)	0.12	0.12	0.19	0.00	0.00	1.29	0.30
Ramachandran plot							
Favored (%)	98.30	98.63	98.56	98.12	96.72	97.40	94.43
Allowed (%)	1.7	1.37	1.44	1.88	3.28	2.60	5.57
Disallowed (%)	0.00	0.00	0.00	0.00	0.00	0.00	0.00

Extended Data Table 1

nature portfolio

Corresponding author(s): Nicholas M.I. Taylor

Last updated by author(s): Nov 19, 2024

Reporting Summary

Nature Portfolio wishes to improve the reproducibility of the work that we publish. This form provides structure for consistency and transparency in reporting. For further information on Nature Portfolio policies, see our Editorial Policies and the Editorial Policy Checklist.

Statistics

For all statistical analyses, confirm that the following items are present in the figure legend, table legend, main text, or Methods section.

n/a	Confirmed	
☐	☒	The exact sample size (*n*) for each experimental group/condition, given as a discrete number and unit of measurement
☐	☒	A statement on whether measurements were taken from distinct samples or whether the same sample was measured repeatedly
☐	☒	The statistical test(s) used AND whether they are one- or two-sided *Only common tests should be described solely by name; describe more complex techniques in the Methods section.*
☒	☐	A description of all covariates tested
☒	☐	A description of any assumptions or corrections, such as tests of normality and adjustment for multiple comparisons
☐	☒	A full description of the statistical parameters including central tendency (e.g. means) or other basic estimates (e.g. regression coefficient) AND variation (e.g. standard deviation) or associated estimates of uncertainty (e.g. confidence intervals)
☐	☒	For null hypothesis testing, the test statistic (e.g. *F*, *t*, *r*) with confidence intervals, effect sizes, degrees of freedom and *P* value noted *Give P values as exact values whenever suitable.*
☒	☐	For Bayesian analysis, information on the choice of priors and Markov chain Monte Carlo settings
☒	☐	For hierarchical and complex designs, identification of the appropriate level for tests and full reporting of outcomes
☒	☐	Estimates of effect sizes (e.g. Cohen's *d*, Pearson's *r*), indicating how they were calculated

Our web collection on statistics for biologists contains articles on many of the points above.

Software and code

Policy information about availability of computer code

Data collection	For cryo-EM: EPU; for TIRF microscopy: NIS-Elements 5.42.04
Data analysis	For cryo-EM: CryoSPARC 4.x, Other: Coot 0.9-pre, Phenix 1.13, Chimera X 1.8, Pymol 2.5.4 and 3.0.2, Bioinformatics Toolkit server (MUSCLE alignment), , MMseqs2, Python 3, ImageJ 1.53t, MicrobeJ 5.13j, GraphPad Prism 9.4.1 and GraphPad Prisim 10. Python code used to generate Extended Data Videos 1 - 6 and plot graphs is available at: https://github.com/SalmoLab/Zorya_Nature2024

For manuscripts utilizing custom algorithms or software that are central to the research but not yet described in published literature, software must be made available to editors and reviewers. We strongly encourage code deposition in a community repository (e.g. GitHub). See the Nature Portfolio guidelines for submitting code & software for further information.

Data

Policy information about availability of data

All manuscripts must include a data availability statement. This statement should provide the following information, where applicable:

- Accession codes, unique identifiers, or web links for publicly available datasets
- A description of any restrictions on data availability
- For clinical datasets or third party data, please ensure that the statement adheres to our policy

Atomic coordinates for ZorAB WT, ZorA_E86A/E89A_ZorB, ZorA_delta_359-592_ZorB and ZorA_delta_435-729_ZorB were deposited in the Protein Data Bank (PDB) under accession codes 8QYD, 8QYH, 8QYK, 8QYY, respectively. The corresponding electrostatic potential maps were deposited in the Electron Microscopy Data Bank (EMDB) under accession codes EMD-18751, EMD-18754, EMD-18756, EMD-18766, respectively. The local refinement map of ZorB PGBD in ZorAB WT were deposited in the EMDB under accession codes EMD-18752. Atomic coordinates for ZorC were deposited in the PDB under accession codes PDB: 8R68. The corresponding electrostatic potential maps was deposited in the EMDB under accession codes EMDB: EMD-18848. Atomic coordinates for ZorD apo form and its complex with ATP-□-S were deposited in the PDB under accession codes PDB: 8QY7 and 8QYC, respectively. The corresponding electrostatic potential maps were deposited in the EMDB under accession codes EMD-18747 and EMD-18750. Official validation reports from wwPDB for all macromolecular structures studied in the paper have been provided. The mass spectrometry proteomics data have been deposited to the ProteomeXchange Consortium via the PRIDE67 partner repository with the dataset identifier PXD047450.

Research involving human participants, their data, or biological material

Policy information about studies with human participants or human data. See also policy information about sex, gender (identity/presentation), and sexual orientation and race, ethnicity and racism.

Reporting on sex and gender	N/A
Reporting on race, ethnicity, or other socially relevant groupings	N/A
Population characteristics	N/A
Recruitment	N/A
Ethics oversight	N/A

Note that full information on the approval of the study protocol must also be provided in the manuscript.

Field-specific reporting

Please select the one below that is the best fit for your research. If you are not sure, read the appropriate sections before making your selection.

☒ Life sciences ☐ Behavioural & social sciences ☐ Ecological, evolutionary & environmental sciences

For a reference copy of the document with all sections, see nature.com/documents/nr-reporting-summary-flat.pdf

Life sciences study design

All studies must disclose on these points even when the disclosure is negative.

Sample size	For cryo-EM: No sample size was calculated. Sample size was based on experience to have a number of micrographs/particles that, if possible, would result in a cryo-EM reconstruction that would allow atomic model construction. For microscopy experiments, no a priori sample sizes were calculated. Sample size were chosen according to our experience concerning quantitative single cell microscopy (e.g. 10.1038/s41467-024-50278-0;10.1073/pnas.2310842120). Exact sample size are provided in the figure legends.
Data exclusions	Junk particles were removed during cryo-EM data processing in CryoSPARC. No microscopy data was excluded from the analysis.
Replication	TIRF: Data derived from at least three independent clones of bacteria and two sets of phage isolations. All attempts at replication were successful. Allocating experimental groups was not relevant for this study, as all bacterial cells of a particular strain are genetic clones. We performed 3 replicates under similar conditions for both the ZorAB full length and ZorB PGBD fragment PG pull-down experiments. The experimental results were consistent. For ZorB PGBD fragment experiments, we selected the experiment with the lowest non-specific binding (as indicated by amount of ZorE pulled down
Randomization	No experimental groups were formed/compared. Data was collected randomly in each set of experiments.
Blinding	Image and data analysis was automated whenever possible. Blinding was neither possible nor necessary for this study, as all bacterial cells of a particular strain are genetic clones and analyses were not sufficiently subjective to require researcher blinding.

Reporting for specific materials, systems and methods

We require information from authors about some types of materials, experimental systems and methods used in many studies. Here, indicate whether each material, system or method listed is relevant to your study. If you are not sure if a list item applies to your research, read the appropriate section before selecting a response.

Materials & experimental systems

n/a	Involved in the study
☐	☒ Antibodies
☒	☐ Eukaryotic cell lines
☒	☐ Palaeontology and archaeology
☒	☐ Animals and other organisms
☒	☐ Clinical data
☒	☐ Dual use research of concern
☒	☐ Plants

Methods

n/a	Involved in the study
☒	☐ ChIP-seq
☒	☐ Flow cytometry
☒	☐ MRI-based neuroimaging

Antibodies

Antibodies used	Promega Anti-Halo Tag Monoclonal Antibody #G921A 1:1,000
Validation	Mouse monoclonal antibody was raised against the Halo Tag protein and validated using E.coli cell lysates expressing Halo Tag as positive control and E.coli lysate not expressing any HaloTag protein as negative control.

Plants

Seed stocks	N/A
Novel plant genotypes	N/A
Authentication	N/A